

The Mean Shape under the Relative Curvature Condition

Mohsen Taheri* , Stephen M. Pizer† and Jörn Schulz‡

April 10, 2024

Abstract

The relative curvature condition (RCC) serves as a crucial constraint, ensuring the avoidance of self-intersection problems in calculating the mean shape over a sample of swept regions. By considering the RCC, this work discusses estimating the mean shape for a class of swept regions called elliptical slabular objects based on a novel shape representation, namely elliptical tube representation (ETRep). The ETRep shape space equipped with extrinsic and intrinsic distances in accordance with object transformation is explained. The intrinsic distance is determined based on the intrinsic skeletal coordinate system of the shape space. Further, calculating the intrinsic mean shape based on the intrinsic distance over a set of ETReps is demonstrated. The proposed intrinsic methodology is applied for the statistical shape analysis to design global and partial hypothesis testing methods to study the hippocampal structure in early Parkinson's disease.

Keywords: Elliptical Tube, Generalized Cylinder, Swept Skeletal Structure, Statistical Shape Analysis, Slabular Objects, Relative Curvature Condition.

*Mohsen Taheri, Department of Mathematics and Physics, University of Stavanger (UiS), Email: mohsen.taherishalmani@uis.no

†Prof. Stephen M. Pizer, Department of Computer Science, University of North Carolina at Chapel Hill (UNC), Email: pizer@cs.unc.edu

‡Assoc. Prof. Jörn Schulz, Department of Mathematics and Physics, University of Stavanger (UiS), Email: jorn.schulz@uis.no

1 Introduction

Object shapes in 3D or 2D are important for statistical analysis, for example, in the characterization of diseases of the human body. Such analysis is commonly based on moments, especially means and covariances, on abstract metric spaces. For these spaces to support these moments, paths on these spaces are best if they pass through only geometrically valid shapes; distances of these paths then form the basis for calculating means and covariances. Here we create such a shape space from an object representation provided by elliptical tubes, which form a useful approximation of so-called slabular objects, and we focus on the calculation of means.

Considering that a variety of human body parts like the kidney, mandible, and hippocampus are slab-shaped *objects* known as *slabular objects* (SIOs) (Pizer et al., 2022; Taheri and Schulz, 2022), calculating the (sample) *mean shape* of such objects is crucial for hypothesis testing and statistical inferences to reveal underlying patterns and differences within SIO groups (e.g., patients vs. controls) (Fletcher et al., 2004; Styner et al., 2006; Schulz et al., 2016; Taheri et al., 2023). However, calculating the SIO mean shape is not straightforward as the mean shape may violate SIO conditions or might be an inappropriate representative of the sample. In this work, we explore the problem and propose a solution for a class of SIOs called *elliptical SIOs* (E-SIOs) by discussing their shape, shape space, and shape distance.

An SIO is a *swept region* based on a smooth sequence of slicing planes along the SIO’s center curve called the *spine* such that the slicing planes do not intersect within the object. Each *cross-section* (i.e., the intersection of a slicing plane with the object) can be seen as a 2-dimensional (2D) *generalized tube*¹ with a (planar) center curve, and the spine of the SIO intersects each cross-section roughly at the midpoint of the cross-section’s center curve.

For a 2D generalized tube, the center curve can be considered as the *skeleton*², and the cross-sections are line segments divided by the skeleton. Thus, each line segment can be seen as two vectors with opposite directions and a common tail position (see Figure 1

¹A generalized tube or a generalized cylinder is a swept region defined by a center curve where each cross-section is a star-convex set such that the center curve intersects a star center of each cross-section (Ballard and Brown, 1982; Damon, 2008; Ma et al., 2018b).

²The skeleton of an object is a curve or a sheet (or a combination of both) that can be understood as a locally centered manifold obtainable by the process of continuous contraction (Siddiqi and Pizer, 2008; Bærentzen and Rotenberg, 2021).

(right)). In this sense, a 2D generalized tube has a *skeletal structure* as a set of non-intersecting vectors called *skeletal spokes* emanating from the skeleton with tails on the skeleton and tips on the boundary. The skeletal structure can be seen as a radial vector field that defines an outward flow from the skeleton to the boundary (Damon, 2003).

Since an SIO is the union of its cross-sections that are 2D generalized tubes, we consider a *swept skeletal structure* for the SIO as the union of the cross-sections’ skeletal structures (Damon, 2008; Taheri et al., 2023). In this sense, SIO’s swept skeletal structure consists of the SIO’s skeleton called the *skeletal sheet* as the union of the cross-sections’ center curves and the vector field on the skeletal sheet as the union of the skeletal spokes.

Theoretically, SIO analysis could be highly challenging because an SIO as a swept region can be tangled like a knot with an extremely complex structure. However, a fraction of SIOs in a human’s body, including most of the brain’s subcortical structures (e.g., hippocampus and caudate nucleus), can be seen as E-SIOs. We define an E-SIO as an SIO that can be properly inscribed inside an optimal *elliptical tube* (E-tube), as we discuss in Section 2, where an E-tube is a 3D generalized tube such that all its cross-sections are elliptical discs with non-zero eccentricity centered at the tube’s center curve. Figure 1 illustrates a swept skeletal structure of the hippocampus as an E-SIO inscribed inside an optimal E-tube.

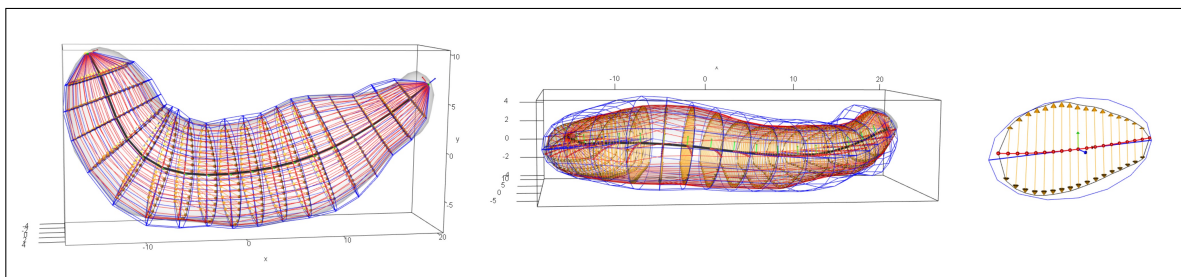


Figure 1: Visualization of a left hippocampus as an E-SIO inscribed inside an optimal E-tube. The right figure illustrates the skeletal structure of a cross-section with its center curve. The skeletal spokes are vectors with tails on the center curve. The cross-section is inscribed inside its corresponding elliptical cross-section of the E-tube.

A suitable shape or *shape representation* should establish locational correspondence among a population of objects based on their common geometric characteristics (Laga et al., 2019). For example, assume a sample of m E-SIOs as $\{P_j\}_{j=1}^m$. In a naive approach, each E-SIO can be represented by a distribution of n points called the *point distribution model* (PDM) on the object’s boundary as the n -tuple $P_j = (\mathbf{p}_{j1}, \dots, \mathbf{p}_{jn})$, where $\forall i \in \{1, \dots, n\}$; $\mathbf{p}_{ji} \in \mathbb{R}^3$ (Styner et al., 2006). That is, the E-SIOs are in a point-wise correspondence. By

assuming that the centroids of the PDMs are located at the origin of the global coordinate system (i.e., shapes are aligned such that $\forall j; \frac{1}{n} \sum_{i=1}^n \mathbf{p}_{ji} = \mathbf{0}$), we can scale and represent each PDM as a unit vector as $\mathbf{p}_j = \frac{\text{vec}(P_j)}{\|\text{vec}(P_j)\|} \in \mathbb{S}^{3n-1}$, where $\mathbb{S}^{3n-1} = \{\mathbf{x} \in \mathbb{R}^{3n} \mid \|\mathbf{x}\| = 1\}$ is the $(n-1)$ -sphere, $\text{vec}(\cdot)$ is the vectorization operator, and $\|\cdot\|$ is the Euclidean norm. Thus, each PDM becomes a point on the hypersphere, namely Kendall’s shape space (Kendall, 1984; Dryden and Mardia, 2016), which is a manifold equipped with the geodesic distance $d_g(\mathbf{x}, \mathbf{y}) = \cos^{-1}(\mathbf{x} \cdot \mathbf{y})$ as the shape distance, where (\cdot) is the dot product (Jung et al., 2012). Therefore, $\{P_j\}_{j=1}^m$ can be seen as a distribution of points $\{\mathbf{p}_j\}_{j=1}^m$ on the manifold, and the mean shape (as the Fréchet mean) is a point on the manifold with the minimum sum of squared geodesic distances to all other points as $\bar{\mathbf{p}} = \text{argmin}_{\mathbf{p} \in \mathbb{S}^{(n-1)}} \frac{1}{m} \sum_{j=1}^m d_g^2(\mathbf{p}_j, \mathbf{p})$ (Pennec et al., 2019).

However, an E-SIO is a swept region with the *relative curvature condition* (RCC) that assures that the cross-sections do not intersect within the object region (Damon, 2008; Ma et al., 2018b). To the best of our knowledge, PDM analysis (as discussed by an example in Supplementary Materials) and almost all common shape analysis methods such as elastic shape analysis (Jermyn et al., 2017), functional shape analysis (Srivastava and Klassen, 2016), Euclidean distance matrix analysis (Lele and Richtsmeier, 2001), persistence homology (Gamble and Heo, 2010), and even common skeletal-based methods (Fletcher et al., 2004; Pizer et al., 2013; Taheri and Schulz, 2022) do not take into account the important property of RCC for calculating the mean shape.

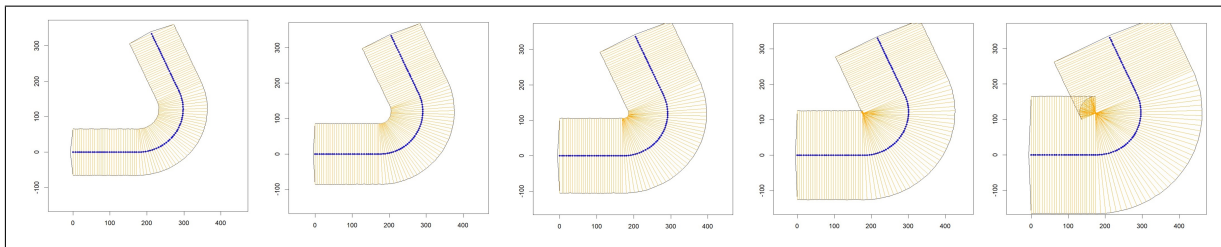


Figure 2: Illustration of the curvature tolerance in 2D. By increasing the object’s width from left to right, the cross-sections intersect within the object by violating RCC, as depicted in the right figure.

As depicted in Figure 2, the RCC defines curvature tolerance for a swept region (e.g., in 2D as $\kappa < \frac{1}{r}$) such that the curvature (κ) of the center curve at each point cannot be larger than the inverse of the object’s width (r) in the direction of the curve’s normal.

Analogously, in E-SIO, the slicing planes intersect within the object if the center curve

violates the RCC (see [Figures 3 and 5](#)). The ultimate objective of this work is to define the shape and shape space for E-SIOs by considering the RCC such that the shape is an element of the shape space, and each element of the space is associated with a valid unique E-SIO that satisfies the RCC. In this sense, by moving from one element to another element of the space along a path, the object corresponding to the first element transforms into the object corresponding to the second element.

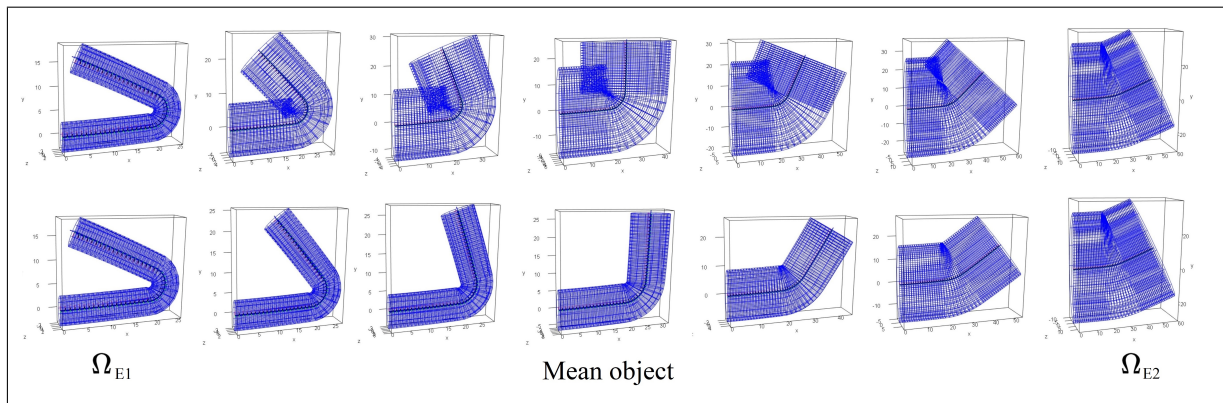


Figure 3: Top row: Extrinsic transformation between the 3D E-tubes Ω_{E1} and Ω_{E2} . Bottom row: Intrinsic transformation between E-tubes Ω_{E1} and Ω_{E2} . The middle column depicts the mean object.

Without considering the RCC, the path can be defined extrinsically. However, we are interested in determining the path intrinsically such that transformation associated with the path does not violate the RCC and the path complies with the structure of the shape space. For a better intuition, imagine two (valid) 3D E-tubes Ω_{E1} and Ω_{E2} (represented by a sequence of elliptical disks), as depicted in [Figure 3](#). The top row shows the extrinsic transformation between Ω_{E1} and Ω_{E2} without considering the RCC based on an extrinsic path between their shapes. The path is invalid because the transformation violates the RCC with an obvious self-intersection. In other words, a part of the extrinsic path is located outside the underlying shape space. The bottom row depicts an intrinsic transformation based on an intrinsic path following the RCC that avoids self-intersection. We discuss the underlying shape space, corresponding paths, and transformations in [Section 4](#). Based on the definition of the path, we can define the (extrinsic or intrinsic shape) distance and the mean shape as a shape with the minimum sum of squared distances to the shapes of Ω_{E1} and Ω_{E2} . We call the object corresponding to the mean shape the *mean object*. The middle column of [Figure 3](#) depicts the E-tube associated with the mean object of Ω_{E1} and Ω_{E2} .

Note that the extrinsic mean object might be a valid object, but it might be an inappropriate representative of the population as its shape does not comply with the boundary condition of the underlying shape space (as discussed by a simple example in Supplementary Materials). Also, we do not consider arbitrary object modifications to remove self-intersections from the mean object, for example, by elongating or narrowing the objects or by smoothing the boundary (Ma et al., 2018a). Such modifications can be considered as arbitrary projections of the invalid shape into the underlying shape space.

To define the shape space and intrinsic path, we need a robust shape representation. Since, for an E-SIO, there is a moving plane along the spine that sweeps the object’s skeletal structure, Taheri et al. (2023) introduced *locally parameterized discrete swept skeletal representations* (LPDSSRep) based on a sequence of orthonormal *material frames* (Yang et al., 2022; Giomi and Mahadevan, 2010) (representing a moving frame) on the E-SIO’s spine with one element tangent to the spine and one element normal to the skeletal sheet (see Figure 4). The LPDSSRep is a powerful shape representation as it is invariant to the act of rigid transformation and alignment-independent (i.e., translation and rotation do not affect the shape representation). Besides, the E-SIO’s boundary can be reconstructed precisely based on the LPDSSRep’s *implied boundary* (i.e., the envelope of the skeletal spokes’ tips). However, considering the RCC, defining the LPDSSRep shape space and intrinsic transformation is not straightforward because of the complex structure of the cross-sections that are 2D generalized tubes. Since each cross-section of an E-SIO can be inscribed and approximated by an ellipse, it seems reasonable to use a simplified version of the LPDSSRep called *elliptical tube representation* (ETRep), where the 2D generalized tube cross-sections are replaced with elliptical disks (see Figures 1 and 4). Thus, the ETRep is an E-SIO representation as a discrete E-tube compatible with the object’s swept skeletal structure, which enables us to explain the shape space and intrinsic transformation explicitly.

The structure of this work is as follows. Section 2 discusses basic terms and definitions regarding the swept skeletal structure. Section 3 explains the discrete material frame that we use to define the ETRep space based on the RCC. Section 4 shows how to calculate the mean shape by demonstrating ETRep model fitting, RCC for ETReps, the ETRep space, skeletal coordinate system, and extrinsic and intrinsic transformations. Section 5 discusses statistical shape analysis of ETRep by applying global and partial hypothesis testings on a

real data set to compare hippocampal differences between patients with Parkinson’s disease versus a control group. Finally, [Section 6](#) summarizes and concludes the work.

2 Basic terms and definitions

In this section, we review some basic terms and definitions regarding E-SIO and the swept skeletal structure essential for defining the ETReps.

The (Cartesian) product space over sets O_1, \dots, O_d is $\{(o_1, \dots, o_d) | \forall i \in \{1, \dots, d\}; o_i \in O_i\}$ denoted by $O_1 \times \dots \times O_d$ or if the sets are identical by $(O_1)^d$. The d -dimensional Euclidean space is the product space $(\mathbb{R})^d$ denoted by \mathbb{R}^d , where \mathbb{R} is the set of real numbers. A point or a vector is an element of $\mathbb{R}^{d>1}$ denoted by small and bold letters. The set $B_r^d(\mathbf{p}) = \{\mathbf{x} \in \mathbb{R}^d | \|\mathbf{x} - \mathbf{p}\| \leq r\}$ defines a d -dimensional closed ball in \mathbb{R}^d with center $\mathbf{p} \in \mathbb{R}^d$ and radius $r \in \mathbb{R}^+$, where $\mathbb{R}^+ = (0, \infty)$. Similarly, a d -dimensional open ball is defined by $B_{<r}^d(\mathbf{p}) = \{\mathbf{x} \in \mathbb{R}^d | \|\mathbf{x} - \mathbf{p}\| < r\}$.

Let the unit closed ball $B_1^d(\mathbf{0})$ be denoted by \mathbb{B}^d . We consider the set $\Omega \subset \mathbb{R}^d$ as a d -dimensional object if it is homeomorphic to \mathbb{B}^d (i.e., there is a continuous invertible mapping between Ω and \mathbb{B}^d ([Gamelin and Greene, 1999](#))). A point $\mathbf{p} \in \Omega$ is an interior point of Ω if $\exists r \in \mathbb{R}^+$ such that $B_r^d(\mathbf{p}) \subset \Omega$. Let Ω_{in} be the set of all interior points of Ω . Then, the boundary of Ω is $\partial\Omega = \Omega/\Omega_{in}$ ([Siddiqi and Pizer, 2008](#)).

Assume an interior point $\mathbf{p} \in \Omega_{in}$ and a unit direction $\mathbf{u} \in \mathbb{S}^{d-1}$. If we start at \mathbf{p} and move straight forward in the direction of \mathbf{u} , we ultimately reach the boundary at a point $\mathbf{q} \in \partial\Omega$. Such an interior path is a line segment called *spoke*, which can be seen as the vector $\overrightarrow{\mathbf{p}\mathbf{q}}$. The set of skeletal spokes of Ω is a set of (non-crossing) spokes emanating from the object’s skeleton denoted by M_Ω . Thus, the *skeletal structure* of Ω is a field of skeletal spokes S on M_Ω denoted by (M_Ω, S) . The envelope of the skeletal spokes’ tips forms the object’s (implied) boundary as $\partial\Omega = \{\mathbf{p} + S(\mathbf{p}) | \mathbf{p} \in M_\Omega\}$, where $S(\mathbf{p})$ is the set of all skeletal spokes with tail on \mathbf{p} ([Damon, 2003](#); [Pizer et al., 2013](#)).

Now, assume $\Gamma(\lambda)$ as a parameterization of a curve Γ in \mathbb{R}^d such that $\lambda \in [0, 1]$, where $\Gamma(0)$ and $\Gamma(1)$ denote the curves’ endpoints. Let $\Pi(\lambda)$ denote a $(d - 1)$ -dimensional plane crossing $\Gamma(\lambda)$ normal to Γ at $\Gamma(\lambda)$. In this work, a d -dimensional object Ω is a swept region with the center curve Γ if Ω is a disjoint union of cross-sections $\Omega(\lambda) = \Omega \cap \Pi(\lambda)$

such that $\forall \lambda$; $\Omega(\lambda)$ is a $(d - 1)$ -dimensional object and $\Gamma(\lambda)$ is a central point (e.g., the barycentroid (Rustamov et al., 2009)) of $\Omega(\lambda)$. The skeletal structure (M_Ω, S) is a *swept skeletal structure* if for each $\mathbf{p} \in \Omega(\lambda) \cap M_\Omega$ we have $S(\mathbf{p}) \subset \Omega(\lambda)$ (Damon, 2008).

A *slab* is a 3D object whose skeleton is a smooth 2D topological disk called the skeletal sheet. An SIO is a slab with a swept skeletal structure such that each cross-section is a 2D generalized tube (Pizer et al., 2022; Taheri et al., 2023). Thus, any E-tube is also an SIO with a *developable*³ skeletal sheet where the center curve of each elliptical cross-section is its major axis (based on the chordal locus of Brady and Asada (1984)). A semi-flat SIO is an SIO whose entire skeletal sheet has relatively low curvature everywhere (i.e., the total curvature of the sheet is close to zero, like an entirely flat surface). For example, a mandible (without considering the coronoid process) is an SIO but not semi-flat, while a hemimandible is a semi-flat SIO (Taheri et al., 2023).

An SIO Ω is an E-SIO if it can be inscribed inside an (optimal) E-tube Ω_E such that $\forall \lambda \in [0, 1]$; $\Omega(\lambda) \subset \Omega_E(\lambda)$ and the SIO’s spine be the E-tube’s spine Γ . Additionally, at each spinal point $\Gamma(\lambda)$, the material frame of both objects coincides (i.e., $\forall \lambda \in [0, 1]$ the skeletal sheets of both objects are tangent at $\Gamma(\lambda)$), and the area of $\Omega_E(\lambda)$ approximates the area of $\Omega(\lambda)$, i.e., the Jaccard index $J(\Omega(\lambda), \Omega_E(\lambda)) = \frac{|\Omega(\lambda) \cap \Omega_E(\lambda)|_A}{|\Omega(\lambda) \cup \Omega_E(\lambda)|_A} \approx 1$, where $|\cdot|_A$ measures the area.

Based on the definition, the swept skeletal structure of an SIO provides insight into whether the object qualifies as an E-SIO. However, calculating the swept skeletal structure of SOs (like the mandible) that are not semi-flat is an open question. Therefore, in this work, we provide examples and study E-SIOs regarding semi-flat SOs. Nevertheless, the theoretical discussions are valid for E-SIOs in general.

3 Discrete moving frame

For statistical shape analysis, we usually consider the swept skeletal structure in the discrete format to establish a meaningful correspondence (Van Kaick et al., 2011) among a population of E-SIOs. The correspondence between different objects can be established by using the curve registration (Srivastava and Klassen, 2016) of the spine and a discrete moving

³A developable surface is a ruled surface that can be swept out by moving a line (Abbena et al., 2017).

frame along the spine. Essentially, this method represents the spine as a finite set of points that correspond with those of other objects. At each spinal point, there is an orthonormal frame that defines the orientation of the cross-section at that point. Consequently, we have a set of corresponding cross-sections. The size, skeletal structure, and orientation of the corresponding cross-sections can be used for comparisons and statistical inferences. Note that without considering the local frames, cross-sectional analysis analogous to the approach of [Apostolova et al. \(2012\)](#) is not desirable as it is alignment-dependent ([Taheri and Schulz, 2022](#)). In this work, we define and use *discrete Frenet frames*⁴ and *discrete material frames* to deal with the RCC in E-SIO analysis.

Assume λ_i as $n + 1$ equally spaced points on $[0, 1]$ as $\lambda_i = \frac{i}{n}$, where $i = 0, \dots, n$. Thus, the spine of an E-SIO can be registered by a sequence of $n + 1$ points $\mathbf{p}_i = \Gamma(\lambda_i)$. We consider the discrete Frenet frame associated with the point \mathbf{p}_i as $T_i = (\mathbf{t}_i, \mathbf{n}_i, \mathbf{n}_i^\perp) \in SO(3)$, where $\mathbf{t}_i = \frac{\mathbf{p}_{i+1} - \mathbf{p}_i}{\|\mathbf{p}_{i+1} - \mathbf{p}_i\|}$, $\mathbf{n}_i^\perp = \frac{\mathbf{t}_{i-1} \times \mathbf{t}_i}{\|\mathbf{t}_{i-1} \times \mathbf{t}_i\|}$, $\mathbf{n}_i = \mathbf{n}_i^\perp \times \mathbf{t}_i$, and $i = 1, \dots, n - 1$ ([Lu, 2013](#)). Thus, \mathbf{n}_i is the normal of the spine at \mathbf{p}_i , which is coplanar with the triangle $\Delta \mathbf{p}_{i-1} \mathbf{p}_i \mathbf{p}_{i+1}$. For the spine's endpoints (i.e., \mathbf{p}_0 and \mathbf{p}_n) we assume $T_0 = T_1$, and $T_n = T_{n-1}$. Since the Frenet frame is sensitive to flipping (specifically when the spine has zero curvature), as noted by [Carroll et al. \(2013\)](#), we use the material frame for establishing correspondence.

Let γ_i be the center curve of the i th cross-section $\Omega(\lambda_i)$. Based on the definition of E-SIO, we have a smooth sequence of cross-sections. Thus, the union $\cup_{i=0}^n \gamma_i$ defines a discrete surface representing the orientable smooth skeletal sheet M_Ω with two sides, namely the *positive* and *negative* sides. We consider a discrete material frame on $\Gamma(\lambda_i)$ consistent with the orientation of M_Ω as $F_i = (\mathbf{t}_i, \mathbf{a}_i, \mathbf{b}_i) \in SO(3)$, where \mathbf{t}_i is the first element of the i th discrete Frenet frame, \mathbf{a}_i is the unit vector tangent to γ_i at \mathbf{p}_i , and $\mathbf{a}_i \times \mathbf{b}_i = \mathbf{t}_i$. Therefore, in an E-tube, \mathbf{a}_i and \mathbf{b}_i are along the semi-major and semi-minor axes of the i th elliptical cross-section, respectively (see [Figure 4](#)). There are two possible options to choose \mathbf{a}_i and \mathbf{b}_i (as an ellipse has two semi-major and two semi-minor axes). We choose F_i such that $\forall i; \mathbf{b}_i$ lies on the positive side of the M_Ω . In other words, (based on the right-hand rule) the orientation induced by the material frame is consistent with the orientation of M_Ω ([Guillemin and Pollack, 2010](#)). We consider F_{i-1} as the parent frame of F_i , where

⁴The Frenet frame, alternatively referred to as the TNB frame, is formed by the combination of the tangent vector, normal vector, and binormal vector of a curve ([do Carmo, 2016](#)).

$i = 1, \dots, n$, and we assume F_0 as the parent of itself.

To calculate the frame orientation based on its parent frame, we use the *spherical rotation matrix* $R(\mathbf{x}, \mathbf{y}) = I_3 + (\sin \psi)(\mathbf{y} \otimes \mathbf{z} - \mathbf{z} \otimes \mathbf{y}) + (\cos \psi - 1)(\mathbf{y} \otimes \mathbf{y} + \mathbf{z} \otimes \mathbf{z})$, where $\mathbf{x}, \mathbf{y} \in \mathbb{S}^2$, $\mathbf{z} = \frac{\mathbf{x} - \mathbf{y}(\mathbf{x} \cdot \mathbf{y})}{\|\mathbf{x} - \mathbf{y}(\mathbf{x} \cdot \mathbf{y})\|}$, $\psi = d_g(\mathbf{x}, \mathbf{y})$, $I_3 = (\mathbf{e}_1, \mathbf{e}_2, \mathbf{e}_3)$ is the identity matrix based on the unit vectors $\mathbf{e}_1 = (1, 0, 0)$, $\mathbf{e}_2 = (0, 1, 0)$, and $\mathbf{e}_3 = (0, 0, 1)$, and \otimes denotes the outer product. Therefore, the rotation $R(\mathbf{x}, \mathbf{y})$ transfers \mathbf{x} to \mathbf{y} along the shortest geodesic path on \mathbb{S}^2 such that $R(\mathbf{x}, \mathbf{y})\mathbf{x} = \mathbf{y}$ (Amaral et al., 2007). Assume frame $F^\dagger = (\mathbf{t}, \mathbf{a}, \mathbf{b})$ be the parent of \tilde{F} . We align F^\dagger to I_3 by $R_2 R_1 F^\dagger = I_3$, where $R_1 = R(\mathbf{t}, \mathbf{e}_1)$, and $R_2 = R(R_1 \mathbf{a}, \mathbf{e}_2)$. Thus, $\tilde{F}^* = R_2 R_1 \tilde{F}$ represents \tilde{F} in its parent coordinate system. Let frame F^* be the orientation of F based on its parent. To find F based on the global coordinate system I_3 , we align F^\dagger to I_3 by $R_2 R_1 F^\dagger = I_3$. Thus, $F = [R_2 R_1]^{-1} F^*$ (Taheri and Schulz, 2022).

The vector $\overrightarrow{\mathbf{p}_{i-1} \mathbf{p}_i}$ called the *ith spinal connection* with length $x_i = \|\overrightarrow{\mathbf{p}_{i-1} \mathbf{p}_i}\|$, connects frame F_i to its parent F_{i-1} . Thus, the spine can be locally parameterized by a sequence of tuples as $((F_i^*, x_i)_{i=0}^n$, where F_i^* is the *ith material frame's orientation* based on its parent frame. Note that by having a locally parameterized spine, we can reconstruct the spine in 3D. Thus, the parameterization also provides Frenet frames. Based on the locally parameterized spine, we define ETRep.

4 ETRep

In Sections 2 and 3, we discussed E-tubes. In this section, we define ETRep as an alignment-independent shape representation for an E-tube. We explain ETRep model fitting based on an optimal E-tube. Then, we discuss the ETRep shape space by explaining the extrinsic and intrinsic paths. To define the intrinsic path, we discuss the RCC for ETReps. Further, we explain the intrinsic sample mean shape based on the intrinsic skeletal coordinate system of the shape space.

4.1 ETRep model fitting

An ETRep is a shape representation. Therefore, we need to discuss the ETRep model fitting procedure to explain how an ETRep represents the actual object.

Let $\Omega_E(\lambda_i)$ be the *ith cross-section* of the E-tube Ω_E with principal radii a_i and b_i .

Since in the discrete format $\Omega_E = \cup_{i=0}^n \Omega_E(\lambda_i)$, we consider the ETRep of Ω_E as the sequence $s = (\omega_i)_{i=0}^n$, where $\omega_i = (F_i^*, x_i, a_i, b_i)$ is the representation of $\Omega_E(\lambda_i)$. Based on the definition, an E-SIO Ω can be inscribed inside an optimal E-tube, as we defined in [Section 2](#). Let Ω_E be the optimal E-tube of Ω . Thus, we consider the shape representation for the Ω as $s = (\omega_i)_{i=0}^n$. In this sense, there is an optimal E-tube for Ω that its shape approximates the shape of Ω .

To find the optimal E-tube of an E-SIO Ω , we calculate the swept skeletal structure of Ω , as discussed by [Taheri et al. \(2023\)](#). Then, we inscribe Ω inside an E-tube $\tilde{\Omega}_E$ such that the spine and material frames of Ω and $\tilde{\Omega}_E$ are the same and $\forall \lambda_i; \Omega(\lambda_i) \subset \tilde{\Omega}_E(\lambda_i)$. Let a_i and b_i be the principal radii of $\tilde{\Omega}_E(\lambda_i)$. The area of each cross-section $\tilde{\Omega}_E(\lambda_i)$ is $\pi a_i b_i$. Since shrinkage of $\tilde{\Omega}_E(\lambda_i)$ does not violate the RCC in $\tilde{\Omega}_E$, we optimize the size of $\tilde{\Omega}_E(\lambda_i)$ by maximizing the Jaccard index $J(\tilde{\Omega}_E(\lambda_i), \Omega_E(\lambda_i))$ (or alternatively by maximizing the multiplication of the Jaccard index and the eccentricity of $\tilde{\Omega}_E(\lambda_i)$). This can be done by (iteratively) reducing the value of a_i and b_i to minimize $a_i b_i$ as much as possible such that (in each iteration) $b_i < a_i$ and $\tilde{\Omega}_E(\lambda_i)$ contains $\Omega(\lambda_i)$ (see [Figure 1](#) (right)). By optimizing all the cross-sections $\forall \lambda_i$, the $\tilde{\Omega}_E$ becomes an optimal E-tube Ω_E for Ω . Note that if Ω cannot be inscribed inside an E-tube or after the optimization $\exists i$ such that $J(\tilde{\Omega}_E(\lambda_i), \Omega_E(\lambda_i))$ is relatively small (e.g., less than 0.8), then we do not consider Ω as an E-SIO. [Figure 4](#) illustrates the ETRep of a hippocampus and a caudate nucleus.

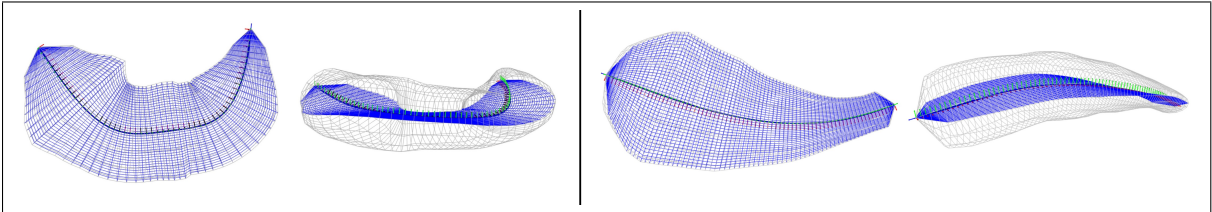


Figure 4: ETRep of a hippocampus (left) and a caudate nucleus (right) in two angles. The spine is depicted by a dark curve equipped with material frames. The cross-sections are non-intersecting elliptical disks. The skeletal sheet is the union of the cross-section's center curves (i.e., their major axes).

4.2 Extrinsic approach

Based on the defined shape representation, we are in the position to discuss shape space and shape distance. In this section, we ignore the RCC and explain the shape space equipped with an extrinsic distance. Afterward, the intrinsic approach will be discussed.

Without considering the RCC, ETRep $s = (\omega_i)_{i=0}^n = ((F_i^*, x_i, a_i, b_i)_i)_{i=0}^n$ is living on the product space $(SO(3) \times (\mathbb{R}^+)^3)^{n+1}$. Assume two ETReps $s_1 = (\omega_{1i})_{i=0}^n$ and $s_2 = (\omega_{2i})_{i=0}^n$ associated with two E-tubes Ω_{E1} and Ω_{E2} , where $\omega_{ji} = (F_{ji}^*, x_{ji}, a_{ji}, b_{ji})_i$, and $j = 1, 2$. Let $\mathbf{f}_{ji}^* \in \mathbb{S}^3$ be the unit quaternion representation of the frame F_{ji}^* (Huynh, 2009). Thus, $s = (\omega_i)_{i=0}^n = (\mathbf{f}_{ji}^*, x_{ji}, a_{ji}, b_{ji})_i$ is living on $\mathbf{S}^{n+1} = (\mathbb{S}^3 \times (\mathbb{R}^+)^3)^{n+1}$, which is a differentiable manifold because it is the product space of finite sets of differentiable manifolds (Lee, 2013; do Carmo, 2016). The extrinsic distance between s_1 and s_2 can be defined as $d_s(s_1, s_2) = \left(\sum_{i=0}^n d_\omega^2(\omega_{1i}, \omega_{2i}) \right)^{\frac{1}{2}}$, where $d_\omega = \left(\sum_{i=0}^n d_g^2(\mathbf{f}_{1i}^*, \mathbf{f}_{2i}^*) + \|x_{1i} - x_{2i}\|^2 + \|a_{1i} - a_{2i}\|^2 + \|b_{1i} - b_{2i}\|^2 \right)^{\frac{1}{2}}$. Thus,

$$d_s(s_1, s_2) = \left(\sum_{i=0}^n d_g^2(\mathbf{f}_{1i}^*, \mathbf{f}_{2i}^*) + \|x_{1i} - x_{2i}\|^2 + \|a_{1i} - a_{2i}\|^2 + \|b_{1i} - b_{2i}\|^2 \right)^{\frac{1}{2}}. \quad (1)$$

We know the geodesic path between \mathbf{f}_{1i}^* and \mathbf{f}_{2i}^* on the unit sphere is

$$\zeta_F(\lambda; \mathbf{f}_{1i}^*, \mathbf{f}_{2i}^*) = \frac{1}{\sin(\psi)} [\sin(\psi(1 - \lambda))\mathbf{f}_{1i}^* + \sin(\lambda\psi)\mathbf{f}_{2i}^*], \quad (2)$$

where $\psi = d_g(\mathbf{f}_{1i}^*, \mathbf{f}_{2i}^*)$, and $\lambda \in [0, 1]$ (Srivastava and Klassen, 2016). We define the extrinsic path from s_1 to s_2 as $\zeta_s(\lambda; s_1, s_2) = (\omega_{\lambda i})_{i=0}^n$ such that

$$\omega_{\lambda i} = (\zeta_F(\lambda; \mathbf{f}_{1i}^*, \mathbf{f}_{2i}^*), \zeta(\lambda; x_{1i}, x_{2i}), \zeta(\lambda; a_{1i}, a_{2i}), \zeta(\lambda; b_{1i}, b_{2i}))_i, \quad (3)$$

where $\forall \mathbf{x}, \mathbf{y} \in \mathbb{R}^d$; $\zeta(\lambda; \mathbf{x}, \mathbf{y}) = (1 - \lambda)\mathbf{x} + \lambda\mathbf{y}$ is a straight path in the Euclidean space \mathbb{R}^d . Thus, the extrinsic transformation is based on an extrinsic path that converts each cross-section of Ω_{E1} to its corresponding cross-section of Ω_{E2} .

In the discrete format, we assume $k + 1$ steps for the transformation. The λ can be considered as the arithmetic sequence $\lambda_j = \frac{j}{k} \in [0, 1]$ (i.e., $0, \frac{1}{k}, \dots, \frac{k-1}{k}, 1$), where $j = 0, \dots, k$. Let $s_{\lambda_j} = \zeta_s(\lambda_j; s_1, s_2)$. Therefore, the distance between s_1 and s_2 can be expressed as $d_s(s_1, s_2) = \lim_{k \rightarrow \infty} \sum_{j=1}^k d_s(s_{\lambda_{j-1}}, s_{\lambda_j})$ (which is identical to Equation (1)).

Given a set of m observations $s_1, \dots, s_m \in \mathbf{S}^{n+1}$. The extrinsic mean shape is

$$\bar{s}_{ext} = \operatorname{argmin}_{s \in \mathbf{S}^{n+1}} \sum_{j=1}^m d_s^2(s, s_j). \quad (4)$$

Following the approach of [Taheri and Schulz \(2022\)](#), the extrinsic sample mean can be calculated as $\bar{s}_{ext} = (\bar{\omega}_i)_{i=0}^n$ such that $\bar{\omega}_i = (\bar{\mathbf{f}}_i^*, \bar{x}_i, \bar{a}_i, \bar{b}_i)_i$, where $\bar{\mathbf{f}}_i^*$ is the mean frame of $\{\bar{\mathbf{f}}_{ji}^*\}_{j=1}^m$ that is obtainable based on *principal nested sphere analysis* (PNS) of [Jung et al. \(2012\)](#) (or alternatively based the approach of [Moakher \(2002\)](#)), and \bar{x}_i , \bar{a}_i , and \bar{b}_i are the arithmetic (or geometric) means of $\{x_{ji}\}_{j=1}^m$, $\{a_{ji}\}_{j=1}^m$, and $\{b_{ji}\}_{j=1}^m$, respectively. Thus, the mean ETRep represents an E-tuple based on the mean of the corresponding cross-sections.

As we mentioned in [Section 1](#), if the extrinsic mean object is invalid, it is almost always possible to make it valid based on object modifications (e.g., by narrowing or elongation). Such arbitrary modifications result in an arbitrary mean shape and unreliable statistics. In other words, any shape in the shape space can be considered the mean shape. On the other hand, even if the mean shape is valid, it does not necessarily comply with the structure of the space, as the extrinsic path ignores the RCC. In fact, based on the extrinsic path, the actual ETRep space is not convex. That is to say, $\exists s_1, s_2 \in \mathcal{A}^{n+1}$, and $\exists \lambda \in (0, 1)$ such that $\zeta_s(\lambda; s_1, s_2) \notin \mathcal{A}^{n+1}$ ([O’Searcoid, 2006](#)), where \mathcal{A}^{n+1} denotes the actual space of ETReps (that we discuss later) by considering RCC.

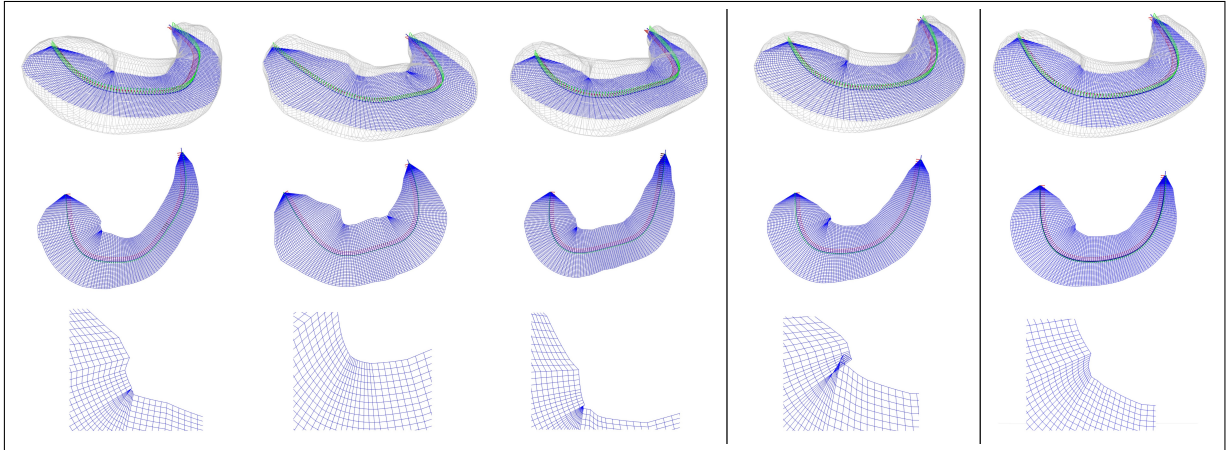


Figure 5: Self-intersecting issue in the mean shape. Left column: Three E-tubes representing three hippocampi. The skeletal sheets are flattened for better visualization. Middle column: The extrinsic mean exhibiting a self-intersection problem. Right column: The intrinsic mean without self-intersection.

[Figure 5](#) (middle column) illustrates the extrinsic mean of three ETRep of three hip-

pocampi with an obvious self-intersection. Although such self-intersections are rare and often considered as artifacts, they reflect that \mathcal{A}^{n+1} is more complicated than \mathbf{S}^{n+1} . By providing an explicit definition for \mathcal{A}^{n+1} , we can follow the idea of [Rustamov et al. \(2009\)](#) to map \mathcal{A}^{n+1} to a convex space, calculate the mean and paths, and transfer them back to \mathcal{A}^{n+1} . [Figure 5](#) (right column) and [Figure 3](#) (bottom row) illustrates such an intrinsic mean and path. To define \mathcal{A}^{n+1} and to explain the intrinsic approach, we discuss the RCC.

4.3 The RCC for discrete E-tubes

In this section, we discuss the RCC for discrete E-tubes based on the fact that each cross-section of an E-tube is an elliptical disk. For simplicity in writing, we denote $\Pi(\lambda_i)$, $\Omega(\lambda_i)$, and $\Gamma(\lambda_i)$ by $\Pi_{(i)}$, $\Omega_{(i)}$, and $\Gamma_{(i)}$, respectively.

For a discrete E-tube Ω_E , we have a sequence of slicing planes $\Pi_{(i)}$, $i = 0, \dots, n$. We consider a local self-intersection at spinal point $\Gamma_{(i)}$ if $\Pi_{(i)}$ intersects with $\Pi_{(i-1)}$ or $\Pi_{(i+1)}$ within Ω_E . Since any two slicing planes of a swept region are adjacent or not adjacent, it is sufficient to discuss the RCC for each slicing plane relative to its previous one. Note that by considering non-local self-intersections, the E-tube space becomes highly complex as we need to define the shape space and an intrinsic path on the shape space of tangled knot-like objects such that object transformation (that can be seen as transforming a tangled knot to another tangled knot) associated with the path does not produce non-local self-intersections. In Supplementary Materials, we provide an iterative algorithm to calculate the Fréchet mean for a class of E-tubes called *simply straightenable* by considering the problem of non-local self-intersection. In this work, we focus on the problem of local self-intersections that can be explored via the RCC, and we leave a detailed study of non-local self-intersections to our future research.

To define shape space based on the RCC, we need to consider the spine curvature. Since there are various ways to define the curvature of a discrete curve ([Vouga, 2014](#)), we take a closer look at the structure of the slicing planes to provide a clear definition of the RCC in the discrete format.

Assume two consecutive cross-sections $\Omega_{(i-1)}$ and $\Omega_{(i)}$ associated with the spinal points $\mathbf{p}_{i-1} = \Gamma_{(i-1)}$ and $\mathbf{p}_i = \Gamma_{(i)}$ of an E-tube with their corresponding material frames F_{i-1}

and F_i , where $F_i = (\mathbf{t}_i, \mathbf{a}_i, \mathbf{b}_i)$ as described in Section 3. Assume $\varphi_i = d_g(\mathbf{t}_{i-1}, \mathbf{t}_i) \in [0, \frac{\pi}{2}]$ as the curvature angle of $\Omega_{(i)}$ based on $R_{\mathbf{n}_i^\perp}(\varphi_i)\mathbf{t}_{i-1} = \mathbf{t}_i$, where $\mathbf{n}_i^\perp = \frac{\mathbf{t}_{i-1} \times \mathbf{t}_i}{\|\mathbf{t}_{i-1} \times \mathbf{t}_i\|}$ and $R_{\mathbf{u}}(\varphi) = I_3 + \sin \varphi [\mathbf{u}]_\times + (1 - \cos \varphi)(\mathbf{u} \otimes \mathbf{u} - I_3)$ is the rotation around axis \mathbf{u} by φ degrees (Lu, 2013). Further, let $\theta_i \in [-\pi, \pi]$ be the twisting angle between \mathbf{a}_i and \mathbf{n}_i relative to \mathbf{t}_i according to the right-hand rule as $R_{\mathbf{t}_i}(\theta_i)\mathbf{a}_i = \mathbf{n}_i$, as depicted in Figure 6.

Assume $\varphi_i \in (0, \frac{\pi}{2}]$, i.e., $\Pi_{(i-1)} \not\parallel \Pi_{(i)}$ (as $\varphi_i \neq 0$). Thus, $\Pi_{(i-1)}$ and $\Pi_{(i)}$ intersect where the intersection is a line orthogonal to \mathbf{t}_{i-1} and \mathbf{t}_i and parallel to $\mathbf{t}_i \times \mathbf{t}_{i-1}$ (Georgiades, 1992). Let point \mathbf{q} be a point on the intersection line with minimum Euclidean distance to \mathbf{p}_i (i.e., $\|\overrightarrow{\mathbf{p}_i \mathbf{q}}\|$ is the radius of a circle on $\Pi_{(i)}$ centered at \mathbf{p}_i tangent to $\Pi_{(i-1)}$). Since the slicing planes cannot intersect within the object, \mathbf{q} must be on the boundary or outside the E-tube Ω_E . Let \mathbf{q}' be an arbitrary point on the intersection line and let $\theta_i = \angle \mathbf{q} \mathbf{p}_i \mathbf{q}'$. Obviously, $\theta_i \in [-\frac{\pi}{2}, \frac{\pi}{2}]$ and the width of $\Omega_{(i)}$ in the direction of $\overrightarrow{\mathbf{p}_i \mathbf{q}}$ cannot exceed $\|\overrightarrow{\mathbf{p}_i \mathbf{q}}\|$. In other words, if \mathbf{q}'' is the boundary point of ω_i along $\overrightarrow{\mathbf{p}_i \mathbf{q}'}$, then $\|\overrightarrow{\mathbf{p}_i \mathbf{q}''}\| \cos \theta_i \leq \|\overrightarrow{\mathbf{p}_i \mathbf{q}}\|$. Let $\kappa_i = \frac{1}{\|\overrightarrow{\mathbf{p}_i \mathbf{q}}\|}$. Then, condition $\|\overrightarrow{\mathbf{p}_i \mathbf{q}''}\| \cos \theta_i \leq \frac{1}{\kappa_i}$ is compatible with RCC in a continuous format (i.e., $r \cos \theta < \frac{1}{\kappa}$) (Damon, 2008). Therefore, the RCC at \mathbf{p}_i can be strictly defined as the maximum possible size of the $\Omega_{(i)}$ such that $\Omega_{(i)}$ does not intersect with $\Pi_{(i-1)}$. Also, we overlook the size of the $\Omega_{(i-1)}$ because if $\Omega_{(i)}$ intersects with $\Pi_{(i-1)}$ without intersecting $\Omega_{(i-1)}$, then the area bounded by the envelope of $\Omega_{(i-1)}$ and $\Omega_{(i)}$ may not be a convex region, which is problematic for defining a smooth implied boundary as the issue produces thorn shape bumps on the implied boundary.

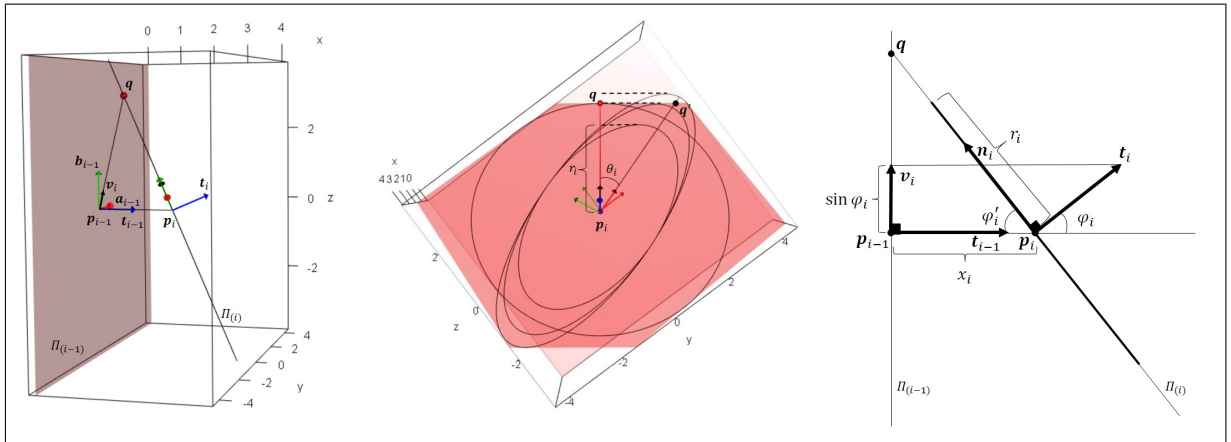


Figure 6: Visualization of two consecutive slicing planes $\Pi_{(i-1)}$ and $\Pi_{(i)}$. Left: Planes crossing \mathbf{p}_{i-1} and \mathbf{p}_i with normals \mathbf{t}_{i-1} and \mathbf{t}_i . Middle: Elliptical cross-sections of different sizes. The largest cross-section violates the RCC. Right: Illustration of a slice of the left and middle figures crossing \mathbf{p}_{i-1} , \mathbf{p}_i , and \mathbf{q} .

The i th cross-section $\Omega_{(i)}$ is an elliptical disk in $\Pi_{(i)}$ centered at \mathbf{p}_i . We apply orthogonal projection to map $\Omega_{(i)}$ on the line $\overleftrightarrow{\mathbf{p}_i\mathbf{q}_i}$. Obviously, the projection is a line segment centered at \mathbf{p}_i with a maximum length of $2\|\overrightarrow{\mathbf{p}_i\mathbf{q}_i}\|$. Let r_i be half the length of the line segment divided by \mathbf{p}_i . Therefore, we have $r_i \leq \|\overrightarrow{\mathbf{p}_i\mathbf{q}_i}\|$. Let $\varphi'_i = \angle \mathbf{p}_i\mathbf{p}_{i-1}\mathbf{q}_i$, and $\varphi_i = \frac{\pi}{2} - \varphi'_i$ be the complement of φ'_i . Thus, $\|\overrightarrow{\mathbf{p}_i\mathbf{q}_i}\| = \frac{x_i}{\cos \varphi'_i}$, and we have $r_i \leq \frac{x_i}{\cos \varphi'_i}$, where $x_i = \|\overrightarrow{\mathbf{p}_{i-1}\mathbf{p}_i}\|$. The RCC of $\Omega_{(i)}$ can be expressed as $r_i \leq \frac{x_i}{\sin \varphi_i}$ (because $\sin \varphi_i = \cos \varphi'_i$). Therefore, given φ_i and x_i , to check whether ω_i complies with the RCC, it is sufficient to calculate r_i . Hence, analogous to the approach of Vouga (2014), the curvature of the discrete curve at \mathbf{p}_i representing the rate of frame rotation can be considered as $\kappa_i = \frac{\sin \varphi_i}{x_i}$.

The boundary of $\Omega_{(i)}$ is an ellipse that can be parameterized as $\partial\Omega_{(i)} = (a_i \cos t, b_i \sin t)$, where $t \in [0, 2\pi]$. By rotating $\partial\Omega_{(i)}$ with θ_i degree clockwise relative to F_i we have

$$\begin{bmatrix} \cos \theta_i & -\sin \theta_i \\ \sin \theta_i & \cos \theta_i \end{bmatrix} \begin{bmatrix} a_i \cos t \\ b_i \sin t \end{bmatrix} = \begin{bmatrix} a_i \cos t \cos \theta_i - b_i \sin t \sin \theta_i \\ a_i \cos t \sin \theta_i + b_i \sin t \cos \theta_i \end{bmatrix}.$$

Thus, $a_i \cos t \cos \theta_i - b_i \sin t \sin \theta_i$ is the parameterized projection of $\partial\omega_i$ onto the line $\overleftrightarrow{\mathbf{p}_i\mathbf{q}_i}$. Assume we have the function $h(t; a, b, \theta) = a \cos t \cos \theta - b \sin t \sin \theta$. For given a_i , b_i , and θ_i , the maximum value of $h(t; a_i, b_i, \theta_i)$ defines r_i . Thus, based on $\frac{\partial h(t; a_i, b_i, \theta_i)}{\partial t} = 0$ we have

$$-a_i \sin t \cos \theta_i - b_i \cos t \sin \theta_i = 0 \Rightarrow \frac{\sin t}{\cos t} = -\frac{b_i \sin \theta_i}{a_i \cos \theta_i} \Rightarrow t = \tan^{-1}\left(\frac{-b_i}{a_i} \tan \theta_i\right).$$

Hence,

$$r_i = \left| a_i \cos\left(\tan^{-1}\left(\frac{-b_i}{a_i} \tan \theta_i\right)\right) \cos \theta_i - b_i \sin\left(\tan^{-1}\left(\frac{-b_i}{a_i} \tan \theta_i\right)\right) \sin \theta_i \right|. \quad (5)$$

Let $s = (\omega_i)_{i=0}^n = ((\mathbf{f}_i^*, x_i, a_i, b_i)_{i=0}^n)$, where ω_i represents $\Omega_{(i)}$. Based on \mathbf{f}_i^* , we can calculate F_i^* of ω_i and consequently the curvature and twisting angles φ_i and θ_i . Thus, by considering the RCC, \mathcal{A}^{n+1} can be seen as a subspace of \mathbf{S}^{n+1} such that if $s \in \mathcal{A}^{n+1}$, then $\forall i; r_i \leq \frac{x_i}{\sin \varphi_i}$, where r_i comes from Equation (5). For a *circular tube* (C-tube) $\forall i$, $\Omega_{(i)}$ is a circle, and we have $r_i = a_i = b_i$. Figure 6 illustrates two slicing planes $\Pi_{(i-1)}$ and $\Pi_{(i)}$ with an elliptical cross-section $\Omega_{(i)}$ of different sizes.

4.4 Semi-intrinsic approach

In this section, we discuss a simple and straightforward approach called the semi-intrinsic approach for defining the ETRep shape space and mean shape. This approach is a modified version of the extrinsic approach discussed in [Section 4.2](#), incorporates the RCC.

Let $s = (\omega_i)_{i=0}^n = ((\mathbf{f}_i^*, x_i, a_i, b_i)_{i=0}^n) \in \mathcal{A}^{n+1}$ and let $\tau_i = \frac{b_i}{a_i} \in (0, 1]$. [Equation \(5\)](#) becomes

$$r_i = |a_i \cos(\tan^{-1}(-\tau_i \tan(\theta_i))) \cos(\theta_i) - \tau_i a_i \sin(\tan^{-1}(-\tau_i \tan(\theta_i))) \sin(\theta_i)|. \quad (6)$$

Since $r_i \leq \frac{x_i}{\sin \varphi_i}$, the ratio $\rho_i = \frac{\tan^{-1}(r_i)}{\tan^{-1}(\frac{x_i}{\sin \varphi_i})}$ is in $(0, 1]$, where $\tan^{-1}(x)$ is a *control function* that maps \mathbb{R}^+ to the finite interval $[0, \frac{\pi}{2}]$. Thus, τ_i reflects the eccentricity of $\Omega_{(i)}$, and ρ_i reflects the ratio of its size relative to its maximum possible size.

Obviously, $r_i = \tan(\rho_i \tan^{-1}(\frac{x_i}{\sin \varphi_i}))$. By replacing r_i in [Equation \(6\)](#) we have

$$a_i = \frac{\tan(\rho_i \tan^{-1}(\frac{x_i}{\sin \varphi_i}))}{|\cos(\tan^{-1}(-\tau_i \tan \theta_i)) \cos \theta_i - \tau_i \sin(\tan^{-1}(-\tau_i \tan \theta_i)) \sin \theta_i|}, \quad (7)$$

and $b_i = \tau_i a_i$.

In fact, we map the non-convex space \mathcal{A}^{n+1} to a convex space, namely $\mathcal{A}^{\dagger n+1}$, by the invertible mapping $\mathcal{F}^\dagger(\mathbf{f}_i^*, x_i, a_i, b_i)_i = (\mathbf{f}_i^*, x_i, \tau_i, \rho_i)_i$, where $\mathcal{A}^\dagger = \mathbb{S}^3 \times \mathbb{R}^+ \times (0, 1]^2$. Thus, ω_i can be represented as $\omega_i^\dagger = (\mathbf{f}_i^*, x_i, \tau_i, \rho_i)_i$ in $\mathcal{A}^{\dagger n+1}$. Assume $s_1^\dagger = ((\mathbf{f}_{1i}^*, x_{1i}, \tau_{1i}, \rho_{1i})_i)_{i=0}^n$ and $s_2^\dagger = ((\mathbf{f}_{2i}^*, x_{2i}, \tau_{2i}, \rho_{2i})_i)_{i=0}^n$. The convexity of $\mathcal{A}^{\dagger n+1}$ can be explained based on a straight path between s_1^\dagger and s_2^\dagger . It is sufficient to replace τ_{ji} and ρ_{ji} with a_{ji} and b_{ji} , in [Equation \(3\)](#), where $j = 1, 2$. Thus, the straight path between s_1^\dagger and s_2^\dagger is

$$\zeta_{s^\dagger}(\lambda; s_1^\dagger, s_2^\dagger) = ((\zeta_F(\lambda; \mathbf{f}_{1i}^*, \mathbf{f}_{2i}^*), \zeta(\lambda; x_{1i}, x_{2i}), \zeta(\lambda; \tau_{1i}, \tau_{2i}), \zeta(\lambda; \rho_{1i}, \rho_{2i}))_i)_{i=0}^n.$$

Thus, $\mathcal{F}^{-1}(\zeta_{s^\dagger}(\lambda; s_1^\dagger, s_2^\dagger))$ is a valid path in \mathcal{A}^{n+1} corresponding to $\zeta_{s^\dagger}(\lambda; s_1^\dagger, s_2^\dagger)$ in $\mathcal{A}^{\dagger n+1}$. The rest of the discussion regarding distance and sample mean is the same as the extrinsic distance and sample mean from [Equation \(1\)](#) and [Equation \(4\)](#). Thus, we have

$$d_{s^\dagger}(s_1^\dagger, s_2^\dagger) = \left(\sum_{i=0}^n d_g^2(\mathbf{f}_{1i}^*, \mathbf{f}_{2i}^*) + \|x_{1i} - x_{2i}\|^2 + \|\tau_{1i} - \tau_{2i}\|^2 + \|\rho_{1i} - \rho_{2i}\|^2 \right)^{\frac{1}{2}},$$

and

$$\bar{s}^\dagger = \operatorname{argmin}_{s^\dagger \in \mathbf{S}_{n+1}^\dagger} \sum_{j=1}^m d_{s^\dagger}^2(s^\dagger, s_j^\dagger).$$

Finally, the sample mean shape is $\mathcal{F}^{-1}(\bar{s}^\dagger)$.

The main concern about the semi-intrinsic approach is defining the control function. There is a variety of functions that can be considered as control functions. For instance, the numerator of Equation (7) changes to the term $(\tan(\rho_i \tan^{-1}(\frac{x_i}{\sin \varphi_i}))^\eta)^{\frac{1}{\eta}}$ by considering the control function as $\tan^{-1}(x^\eta)$, where $\eta \in (0, \infty)$. Therefore, as depicted in Figure 7, the semi-intrinsic transformation and the mean object are very sensitive to the selection of the control function. On the other hand, in the semi-intrinsic approach, the rotation of the cross-section is not commensurate with its size during the transformation. Besides, the structure of the shape space is not explicit.

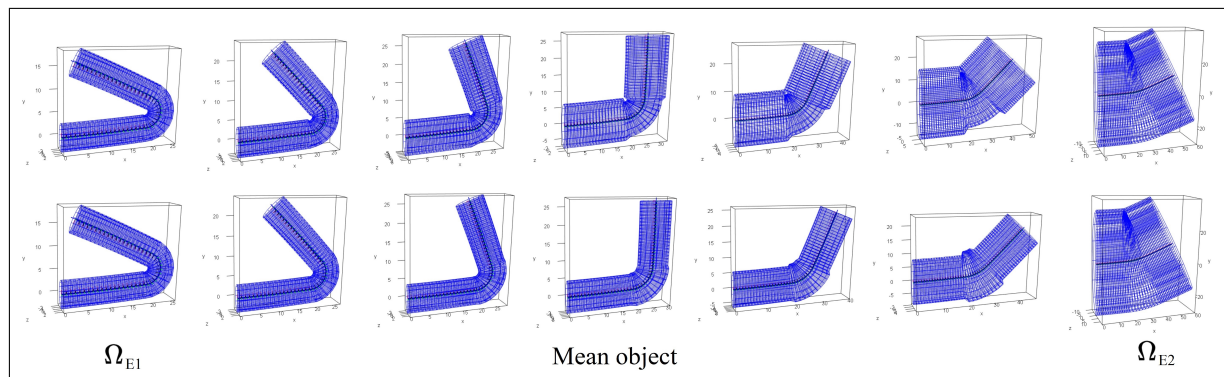


Figure 7: Top row: The semi-intrinsic transformation between E-tubes Ω_{E1} and Ω_{E2} based on the control function $\tan^{-1}(x^\eta)$, wherein the top row η is 0.8, and in the bottom row η is 2.

To explain the ETRep space in the semi-intrinsic approach, we considered the RCC as the maximum size of the cross-section $\Omega_{(i)}$ based on its curvature angle φ_i . That is to say, what the maximum size of $\Omega_{(i)}$ could be based on a given φ_i . To commensurate the rotation of $\Omega_{(i)}$ (i.e., rotation of the material frame) with the size of $\Omega_{(i)}$, we propose a shape space and intrinsic path by considering the RCC as the maximum value of φ_i based on the given $\Omega_{(i)}$. To provide an explicit intuition about the structure of the space, first, we discuss the shape space for C-tubes.

4.5 C-tube shape space

This section discusses the shape space of C-tubes (with circular cross-sections) based on the fact that a C-tube can be seen as an E-tube with infinitesimal cross-sectional eccentricity. Afterward, [Section 4.6](#) generalizes the discussion of this section to propose an intrinsic approach for calculating the mean shape of a sample of ETReps.

As discussed in [Section 4.3](#), in an ETRep $s = ((F_i^*, x_i, a_i, b_i))_{i=0}^n, \forall i \in \{1, \dots, n\}$ vectors $\mathbf{t}_i, \mathbf{t}_{i-1}, \mathbf{n}_i$ are coplanar. Thus we have, $\sin \varphi_i = \|\mathbf{v}_i\|$, where \mathbf{v}_i is the projection of \mathbf{t}_i on $\Pi_{(i-1)}$, as depicted in [Figure 6](#) (Left and Right). The RCC of $\Omega_{(i)}$ can be expressed as $\|\mathbf{v}_i\| \leq \min\{1, \frac{x_i}{r_i}\}$, where r_i comes from [Equation \(5\)](#). If $x_i \geq r_i$ then $\|\mathbf{v}_i\|$ can take any value in $[0, 1]$; also, if $\theta_i = 0$ then $\|\mathbf{v}_i\| \leq \min\{1, \frac{x_i}{a_i}\}$, and if $\theta_i = \pm \frac{\pi}{2}$ then $\|\mathbf{v}_i\| \leq \min\{1, \frac{x_i}{b_i}\}$, as discussed in [Section 4.3](#). In this sense, based on the size of r_i we impose bending restriction on c_i such that $\|\mathbf{v}_i\|$ cannot exceed $\frac{x_i}{r_i}$.

By considering very small but not zero eccentricity for all the cross-sections of a discrete E-tube, we have $\forall i; a_i \simeq b_i \simeq r_i$ (but not equal). In fact, a C-tube can be seen as an E-tube with a skeletal sheet equipped with material frames. Thus, the ETRep becomes the representation of a C-tube that we call CTRep, denoted by $s_c = ((F_i^*, x_i, r_i))_{i=0}^n$, where r_i is the radius of the i th cross-section. Thus, the RCC is $\|\mathbf{v}_i\| \leq \min\{1, \frac{x_i}{r_i}\}$.

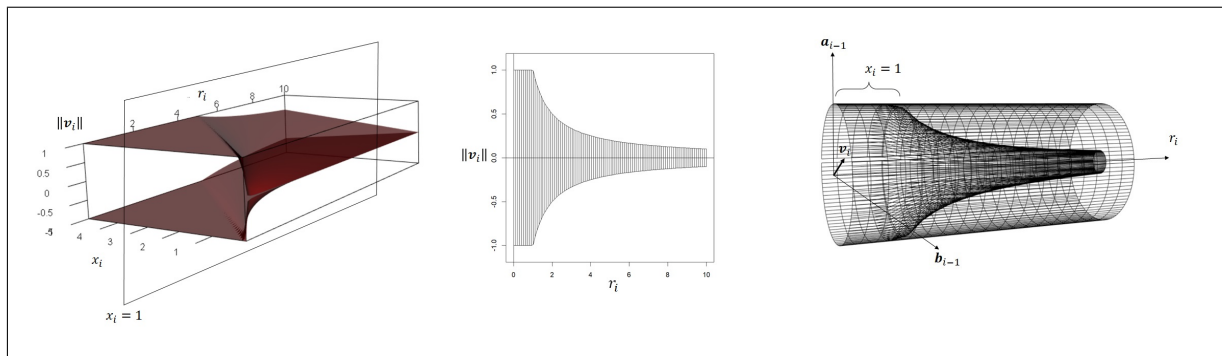


Figure 8: Left: Illustration of \mathcal{A}_{c_2} . Middle: The swept skeletal structure of a slice of \mathcal{A}_{c_2} based on $x_i = 1$. Right: A slice of \mathcal{A}_c based on $x_i = 1$ located inside a convex cylinder with radius 1.0.

In 2D we have $F_i^* = (\mathbf{t}_i, \mathbf{a}_i) \in SO(2)$. Thus, \mathbf{v}_i has one scalar element $v_i \in [-1, 1] = \mathbb{B}$. The i th cross-section $\Omega_{(i)}$ can be represented by the vector $\boldsymbol{\omega}_i = (v_i, x_i, r_i) \in \mathcal{A}_{c_2}$, where $\mathcal{A}_{c_2} \subset \mathbb{R}^3$ is a 3D hyperbolic space such that if $(v, x, r) \in \mathcal{A}_{c_2}$, then $v \in [-1, 1], r, x \in \mathbb{R}^+$, and $|v| \leq \min\{1, \frac{x}{r}\}$. In 3D, $\Omega_{(i)}$ can be represented as $\boldsymbol{\omega}_i = (v_{i1}, v_{i2}, x_i, r_i) \in \mathcal{A}_c$, where $\mathcal{A}_c \subset \mathbb{R}^4$ is a 4D hyperbolic space such that if $(v_1, v_2, x, r) \in \mathcal{A}_c$, then $(v_1, v_2) \in \mathbb{B}^2$,

$r, x \in \mathbb{R}^+$, and $\|(v_1, v_2)\| \leq \min\{1, \frac{x}{r}\}$. Thus, the CTRep with $n + 1$ cross-sections lives on the product space $(\mathcal{A}_c)^{n+1}$, which we denote by \mathcal{A}_c^{n+1} . [Figure 8](#) (left) illustrates \mathcal{A}_{c_2} . [Figure 8](#) (middle) depicts a slice of \mathcal{A}_{c_2} by considering $x_i = 1$ (with its swept skeletal structure). The visualization of \mathcal{A}_c is challenging as it is a 4D space. Analogous to the middle figure, by considering $x_i = 1$, [Figure 8](#) (right) depicts a slice of \mathcal{A}_c , which is a non-convex 3D hyperbolic area located inside a convex region as a cylinder with radius 1.0.

Each slice of \mathcal{A}_c is symmetric relative to the r_i axis. Therefore, each slice is a C-tube with a swept skeletal structure. In this sense, the product space \mathcal{A}_c^{n+1} is a combination of swept regions with swept skeletal structures. Since any point inside a swept region with a swept skeletal structure has an intrinsic *skeletal coordinate*, analogous to the approach of [Pizer et al. \(2022\)](#), we can consider an intrinsic skeletal coordinate system for \mathcal{A}_c^{n+1} . To elaborate further, we discuss *the skeletal coordinate system*.

4.5.1 Skeletal coordinate system

The skeletal coordinate system is an intrinsic coordinate system that can be established based on the skeletal structure of the space ([Pizer et al., 2022](#)). This section explains the skeletal coordinate system for spaces with swept skeletal structures.

Let Ω_E be a 3D E-tube with the parameterized spine $\Gamma(\lambda)$ based on the curve length parameterization. Thus, λ can be seen as the proportion of the curve length at $\Gamma(\lambda)$ from the starting point $\Gamma(0)$ relative to the total length of the curve. Assume $\mathbf{p}_\lambda = \Gamma(\lambda)$, and let $F_\lambda = (\mathbf{t}_\lambda, \mathbf{a}_\lambda, \mathbf{b}_\lambda)$ be the material frame at \mathbf{p}_λ . For any interior point of a swept region with a swept skeletal structure, there is a unique skeletal spoke crossing the point and connecting the Γ to the boundary ([Damon, 2008](#)). Let \mathbf{p} be an interior point of Ω_E . Without loss of generality, let $\overrightarrow{\mathbf{p}_\lambda \mathbf{q}}$ be the direction of the skeletal spoke crossing \mathbf{p} such that $\mathbf{q} \in \partial\Omega_E$. Thus, $\mathbf{p} = \mathbf{p}_\lambda + \varsigma_1 \overrightarrow{\mathbf{p}_\lambda \mathbf{q}}$, where $\varsigma_1 = \frac{\|\overrightarrow{\mathbf{p}_\lambda \mathbf{p}}\|}{\|\overrightarrow{\mathbf{p}_\lambda \mathbf{q}}\|} \in [0, 1]$. Therefore, \mathbf{p} can be represented by the tuple $(\lambda, \varsigma_1 \overrightarrow{\mathbf{p}_\lambda \mathbf{q}})$. Since vector $\varsigma_1 \overrightarrow{\mathbf{p}_\lambda \mathbf{q}}$ is coplanar with \mathbf{a}_λ and \mathbf{b}_λ , by assuming ς_2 as the clockwise angle between \mathbf{a}_λ and $\varsigma_1 \overrightarrow{\mathbf{p}_\lambda \mathbf{q}}$ relative to \mathbf{t}_λ based on the right-hand rule, the direction of \mathbf{v} relative to F_λ can be represented by $\varsigma_2 \in [-\pi, \pi]$ such that $\varsigma_1 \overrightarrow{\mathbf{p}_\lambda \mathbf{q}} = R_{\mathbf{t}_\lambda}(\varsigma_2) \mathbf{a}_\lambda$. Thus, given the spine Γ , any interior point \mathbf{p} can be represented as a unique vector $(\lambda, \varsigma_1, \varsigma_2)$ in $[0, 1] \times [0, 1] \times [-\pi, \pi]$. Besides, for the given $(\lambda, \varsigma_1, \varsigma_2)$, there is a unique skeletal spoke with the tail at $\Gamma(\lambda) = \mathbf{p}_\lambda$ and the direction $R_{\mathbf{t}_\lambda}(\varsigma_2) \mathbf{a}_\lambda$,

which is identical to the direction of $\varsigma_1 \overrightarrow{p_\lambda \hat{q}}$. Thus, the tip of the skeletal spoke is at \mathbf{q} . Therefore, $(\lambda, \varsigma_1, \varsigma_2)$ corresponds to the point $\mathbf{p} = \mathbf{p}_\lambda + \varsigma_1 \overrightarrow{p_\lambda \hat{q}} \in \Omega$. Hence, there is a bijective mapping $\mathcal{F}_s : \Omega_E \rightarrow [0, 1] \times [0, 1] \times [-\pi, \pi]$. Note that in 2D, we do not have ς_2 as the local frame associated with λ belongs to $SO(2)$. Thus, \mathbf{p} can simply be represented as the vector $(\lambda, \pm\varsigma_1)$ in the product space $[0, 1] \times [-1, 1]$. The same discussion is valid for the generalized tubes by considering the local frames as the Frenet frames.

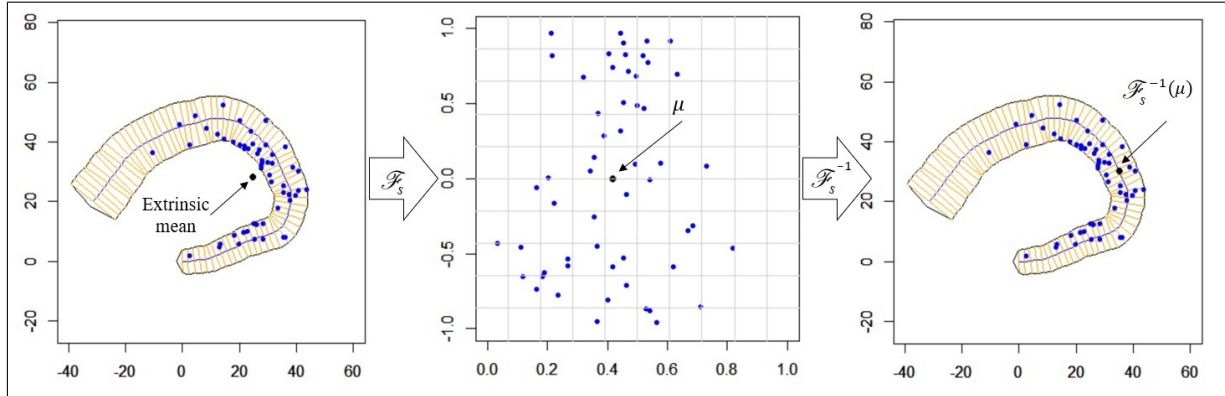


Figure 9: Left: A distribution of points inside a 2D C-tube with a swept skeletal structure. The bold dot is the extrinsic mean, which is outside the region. Middle: The mapped distribution to the product space and the Euclidean mean μ inside the product space. Right: Intrinsic mean as $\mathcal{F}_s^{-1}(\mu)$ depicted as a bold dot which is inside the C-tube.

Since the product space is convex, given a distribution of points $\mathbf{p}_1, \dots, \mathbf{p}_m$ in Ω_E , the intrinsic mean can be considered as $\mathcal{F}_s^{-1}(\mu)$, where μ is the Euclidean mean of $\mathcal{F}_s(\mathbf{p}_1), \dots, \mathcal{F}_s(\mathbf{p}_m)$. Figure 9 (left) depicts a distribution of points inside a 2D C-tube with the Euclidean mean (as the extrinsic mean) that is located outside the region. Figure 9 (middle) illustrates the mapped distribution to the product space and the Euclidean mean μ inside the product space. Figure 9 (right) shows the intrinsic mean as $\mathcal{F}_s^{-1}(\mu)$ inside the C-tube.

A C-tube can be seen as an E-tube with infinitesimal eccentricity in all the cross-sections, i.e., $\forall \lambda; a_\lambda \simeq b_\lambda$. Let $\mathcal{A}_c(x_i)$ be a slice of \mathcal{A}_c at x_i , as depicted in Figure 8 (middle and right). $\mathcal{A}_c(x_i)$ is a C-tube with a straight spine, namely the axis r_i . Thus, the material frames similar to the Frenet frames can be considered as $I_3 = (\mathbf{e}_1, \mathbf{e}_2, \mathbf{e}_3)$ along the spine (i.e., the material frames coincide with the Frenet frames). By considering a large number $R \gg 1$ such that $\forall i; r_i < R$, $\mathcal{A}_c(x_i)$ has a finite spine with an intrinsic skeletal coordinate system. However, $\mathcal{A}_c(x_i)$ is not finite. Nevertheless, it can be seen as an infinite swept

region with a straight infinite spine such that each cross-section is a circular disk.

Therefore, each point $\mathbf{p} = (v_1, v_2, r) \in \mathcal{A}_c(x_i) \subset \mathbb{R}^3$ is located on a skeletal spoke $\overrightarrow{\mathbf{p}_r \mathbf{q}}$ with tail at $\mathbf{p}_r = (0, 0, r)$ and tip at $\mathbf{q} = (\min\{1, \frac{x}{r}\}u_1, \min\{1, \frac{x}{r}\}u_2, r)$ with direction $\mathbf{u} = \frac{\mathbf{v}}{\|\mathbf{v}\|}$, where $\mathbf{v} = (v_1, v_2, 0)$. Thus, $\mathbf{p} = \mathbf{p}_r + \varsigma_1 \overrightarrow{\mathbf{p}_r \mathbf{q}}$, where $\varsigma_1 = \frac{\|\mathbf{v}\|}{\|\overrightarrow{\mathbf{p}_r \mathbf{q}}\|} = \frac{\sqrt{v_1^2 + v_2^2}}{\min\{1, \frac{x}{r}\}} \in [0, 1]$. Hence, \mathbf{p} can be represented based on a cylindrical coordinate as $\mathcal{F}_s(\mathbf{p}) = (\varsigma_1 \cos \varsigma_2, \varsigma_1 \sin \varsigma_2, r)$, where $\varsigma_2 \in [-\pi, \pi]$ is the clockwise angle between \mathbf{e}_2 and \mathbf{v} . Since \mathbf{u} and \mathbf{v} have the same direction, we have $\mathcal{F}_s(\mathbf{p}) = (\varsigma_1 u_1, \varsigma_1 u_2, r)$ or more explicitly as $\mathcal{F}_s(\mathbf{p}) = (\varsigma_1 \mathbf{u}, r)$ in the convex cylinder $\mathbb{B}^2 \times \mathbb{R}^+$, as illustrated in [Figure 8](#) (right). In other words, \mathcal{F}_s can be seen as the bijective mapping $\mathcal{F}_s : \mathcal{A}_c(x_i) \rightarrow \mathbb{B}^2 \times \mathbb{R}^+$.

Based on the fact that \mathcal{A}_c is a combination of its slices and by considering that the mapping $\mathcal{F}_s(\mathbf{p})$ acts on the first two elements of \mathbf{p} , any arbitrary point $\boldsymbol{\omega} = (v_1, v_2, x, r)$ (representing a cross-section) inside \mathcal{A}_c can be represented as an element of the convex 4D product space $\widehat{\mathcal{A}}_c = \mathbb{B}^2 \times (\mathbb{R}^+)^2$ as $\mathcal{F}_s(\boldsymbol{\omega}) = (\varsigma_1 \mathbf{u}, x, r)$ (based on the skeletal coordinate system of the slice that $\boldsymbol{\omega}$ belongs to), i.e., $\mathcal{F}_s : \mathcal{A}_c \rightarrow \widehat{\mathcal{A}}_c$ is a bijective mapping. The same discussion is valid if we consider the slices based on the r -axis. In this sense, the plane expanded by the x and r axes can be seen as the skeletal sheet of \mathcal{A}_c (see [Figure 8](#) (left)).

4.6 Intrinsic approach

Let $\mathcal{A}_e \subset \mathbb{R}^6$ be the space of elliptical cross-sections $\boldsymbol{\omega} = (v_1, v_2, \theta, x, a, b) \in \mathcal{A}_e$, where $\mathbf{v} = (v_1, v_2) \in \mathbb{B}^2$, $a, b, x \in \mathbb{R}^+$, $\theta \in [-\pi, \pi]$, $a \geq b$, and the condition $\|\mathbf{v}\| \leq \min\{1, \frac{x}{r}\}$ associated with RCC is satisfied, where r comes from [Equation \(5\)](#) (by considering (a_i, b_i, θ_i) as (a, b, θ)). Thus, $\boldsymbol{\omega}$ can be considered as a representation of an elliptical cross-section. Obviously, the concavity of \mathcal{A}_e comes from the condition $\|\mathbf{v}\| \leq \min\{1, \frac{x}{r}\}$ as by ignoring this condition $\boldsymbol{\omega}$ can be represented by $\boldsymbol{\omega} = (\mathbf{v}, \theta, x, a, b)$ belongs to the convex product space $\widehat{\mathcal{A}}_e = \mathbb{B}^2 \times [-\pi, \pi] \times (\mathbb{R}^+)^3$. Therefore, analogous to \mathcal{A}_c , we consider an intrinsic skeletal coordinate for $\boldsymbol{\omega}$ (based on the mapping \mathcal{F}_s) as $\mathcal{F}_s(\boldsymbol{\omega}) = (\varsigma_1 \mathbf{u}, \theta, x, a, b) \in \widehat{\mathcal{A}}_e$, where $\varsigma_1 = \frac{\|\mathbf{v}\|}{\min\{1, \frac{x}{r}\}}$ and $\mathbf{u} = \frac{\mathbf{v}}{\|\mathbf{v}\|}$ (intuitively, there is a skeletal spoke with tail and tip at $(0, 0, \theta, x, a, b)$ and $(\min\{1, \frac{x}{r}\}u_1, \min\{1, \frac{x}{r}\}u_2, \theta, x, a, b)$). Thus, $\mathcal{F}_s(\boldsymbol{\omega}) : \mathcal{A}_e \rightarrow \widehat{\mathcal{A}}_e$, and we consider intrinsic coordinate systems for \mathcal{A}_e and for the product space $(\mathcal{A}_e)^{n+1}$. We denote $(\mathcal{A}_e)^{n+1}$ by \mathcal{A}_e^{n+1} and its corresponding convex space $(\mathcal{F}_s(\mathcal{A}_e))^{n+1}$ by $\widehat{\mathcal{A}}_e^{n+1}$.

By representing ETRep as $\mathcal{F}_s(s) = ((\varsigma_{1i}\mathbf{u}_i, \theta_i, x_i, a_i, b_i)_{i=0}^n)$ in $\widehat{\mathcal{A}}_e^{n+1}$, we can reconstruct the E-tube associated with s in 3D. Since $\forall i; (v_{i1}, v_{i2}) = \min\{1, \frac{x_i}{r_i}\}\varsigma_{1i}\mathbf{u}_i$, we calculate the i th tangent vector based on its parent frame (which is the $(i-1)$ th material frame) as $\mathbf{t}_i = (\sqrt{1 - v_{i1}^2 - v_{i2}^2}, v_{i1}, v_{i2})$. Thus, by considering the geodesic path on the unit sphere from Equation (2), we obtain the i th Frenet frame based on its parent frame as $T_i^* = (\mathbf{t}_i, \mathbf{n}_i, \mathbf{n}_i^\perp)$, where $\mathbf{n}_i^\perp = \frac{1}{\sin\psi}(-\mathbf{e}_1 + \sin(\psi - \frac{\pi}{2})\mathbf{t}_i)$, $\psi = d_g(-\mathbf{e}_1, \mathbf{t}_i)$, and $\mathbf{n}_i = \mathbf{n}_i^\perp \times \mathbf{t}_i$. Consequently, the i th material frame based on its parent is $F_i^* = (\mathbf{t}_i, \mathbf{a}_i, \mathbf{b}_i)$, where $\mathbf{a}_i = R_{\mathbf{t}_i}(-\theta_i)\mathbf{n}_i$, and $\mathbf{b}_i = \mathbf{t}_i \times \mathbf{a}_i$. Since x_i provides the distance between the frames, by assuming $T_0 = F_0 = I_3$, we can obtain the spine by calculating the material frames in the global coordinate system as discussed in Section 3. Finally, a_i and b_i define the size of the i th cross-section.

Assume ETReps $s_1 = (\boldsymbol{\omega}_{1i})_{i=0}^n$ and $s_2 = (\boldsymbol{\omega}_{2i})_{i=0}^n$ in \mathcal{A}_e^{n+1} . We define the intrinsic path between s_1 and s_2 as $\zeta_I(\lambda, s_1, s_2) = (\mathcal{F}_s^{-1}(\zeta(\lambda, \mathcal{F}_s(\boldsymbol{\omega}_{1i}), \mathcal{F}_s(\boldsymbol{\omega}_{2i}))))_{i=0}^n$. Let s_1, \dots, s_m as a set of ETReps. By assuming the intrinsic distance as the Euclidean distance in the convex space $\widehat{\mathcal{A}}_e^{n+1}$, the intrinsic mean is the inverse map of the Euclidean mean of the mapped shapes as $\bar{s} = \mathcal{F}_s^{-1}(\frac{1}{m} \sum_{j=1}^m \mathcal{F}_s(s_j))$. Figure 10 illustrates the intrinsic mean object of a set of arbitrary 3D E-Tubes. For better visualization, the E-Tubes are aligned based on their initial material frames.

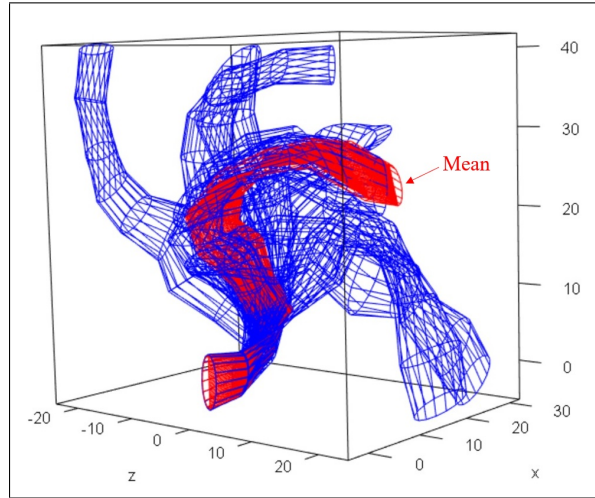


Figure 10: The intrinsic mean object of ten 3D E-tubes, which need not be aligned.

5 Application

One significant application of sample mean shape is in studying shape differences based on hypothesis testing. In this section, we discuss ETRep hypothesis testing based on the intrinsic approach of [Section 4.6](#) using a hippocampal data set provided by the Stavanger University Hospital from the ParkWest study ([Alves et al., 2009](#)). In the Supplementary Materials, the same data set is used to examine hypothesis testing through the semi-intrinsic approach of [Section 4.4](#).

The ETRep intrinsic representation is invariant to the act of rigid transformation. For the statistical shape analysis, we need to remove the scale. Assume an ETRep $s = ((\varsigma_1 u_{1i}, \varsigma_1 u_{2i}, \theta_i, x_i, a_i, b_i)_{i=0}^n) \in \widehat{\mathcal{A}}_e^{n+1}$. Following [Taheri and Schulz \(2022\)](#), we have $\ell = \exp\left(\frac{1}{3n+2}(\sum_{i=1}^n \ln x_i + \sum_{i=0}^n \ln a_i + \sum_{i=0}^n \ln b_i)\right)$ as the *LP-size* of s . Thus, the scaled and vectorized form of s is a vector $\mathbf{s} = (\varsigma_1 u_{1i}|_{i=0}^n, \varsigma_1 u_{2i}|_{i=0}^n, \theta_i|_{i=0}^n, \frac{x_i}{\ell}|_{i=0}^n, \frac{a_i}{\ell}|_{i=0}^n, \frac{b_i}{\ell}|_{i=0}^n)$ living on the convex feature space $(\mathbb{B})^{2(n+1)} \times ([-\pi, \pi])^{n+1} \times (\mathbb{R}^+)^{3(n+1)} \subset \mathbb{R}^{6(n+1)}$.

Let $A = \{\mathbf{s}_{Aj}\}_{j=1}^{m_1}$ and $B = \{\mathbf{s}_{Bj}\}_{j=1}^{m_2}$ be two groups of scaled ETReps of sizes m_1 and m_2 . Since each ETRep is represented as a vector. The global test can be considered as $H_0 : \mu_A = \mu_B$ versus $H_{1k} : \mu_A \neq \mu_B$ where μ_A and μ_B are the observed Euclidean sample means in the convex feature space. For the hypothesis testing, we consider the permutation test with minimal assumption. Given the pooled group of two data sets (here $A \cup B$), the permutation method randomly partitions the pooled group into two groups of sizes m_1 and m_2 without replacement many times and measures the test statistic between the paired groups. The empirical p -value is $\eta = \frac{1 + \sum_{h=1}^L \chi_I(|t_h| \geq |t_o|)}{L+1}$ ([Rizzo, 2007](#)), where t_o is the observed test statistics (e.g., Hotelling's T^2 metric $T^2 = (\bar{\mathbf{x}} - \bar{\mathbf{y}})^T \hat{\Sigma}^{-1} (\bar{\mathbf{x}} - \bar{\mathbf{y}})$, where $\hat{\Sigma}$ is the common covariance matrix ([Mardia et al., 1982](#))), t_h is the h th permutation test statistic, L is the number of permutation (usually greater than 10^4), and χ_I is the indicator function (i.e., $\chi_I(\varphi) = 1$ if φ is true, otherwise $\chi_I(\varphi) = 0$) ([Taheri and Schulz, 2022](#)). Since in ETRep analysis, the feature space is a high dimensional space, for the global test, we considered the *direction projection permutation* (DiProPerm) method of [Wei et al. \(2016\)](#).

Further, to detect local dissimilarities, we compare ETReps element-wise based on partial permutation tests $H_{0k} : \mu_A(k) = \mu_B(k)$ versus $H_{1k} : \mu_A(k) \neq \mu_B(k)$ based on the test statistic as t-statistic (i.e., $t = \frac{\bar{x} - \bar{y}}{\hat{\sigma}_p \sqrt{\frac{1}{m_1} + \frac{1}{m_2}}}$), where $\mu_A(k)$ and $\mu_B(k)$ are the observed

sample mean of the k th feature, and $k = 1, \dots, 6(n+1)$. Since the partial tests are multiple comparisons, to control false positives, we adjust p -values using the *false discovery rate* (FDR) of [Benjamini and Hochberg \(1995\)](#). [Figures 11 and 12](#) illustrate the result of the



Figure 11: Global test based on DiProPerm. Left: DiProPerm projection score of the observed distributions. Class labels -1 and 1 are associated with CG and PD. Right: The permutation statistics.

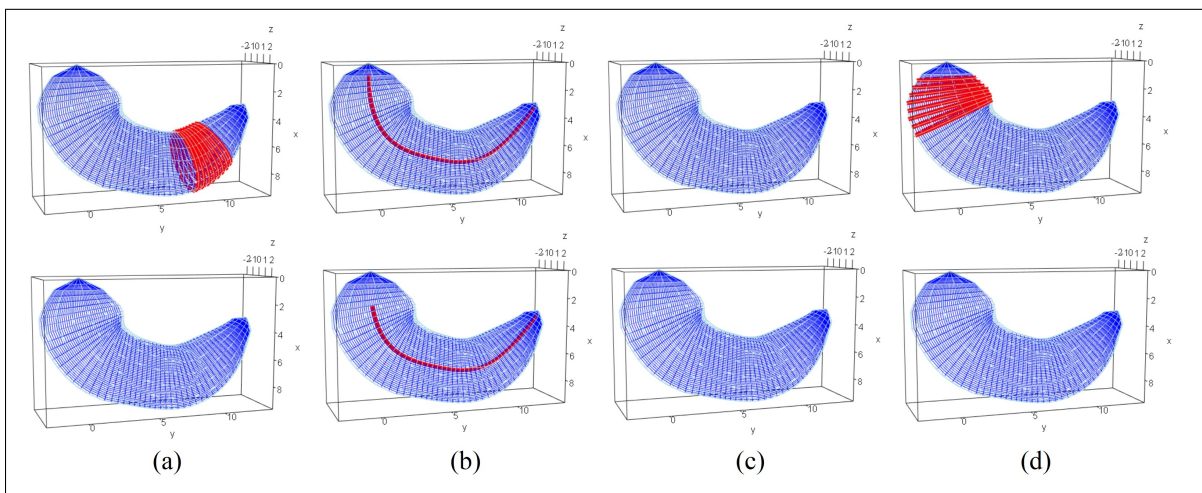


Figure 12: Hypothesis testing based on the significant level $\alpha = 0.1$. The top row depicts significant features based on raw p -values. The bottom row shows significant features after p -value adjustment with $FDR = 0.1$. Significant features are highlighted in bold where columns (a-d) depict significant sizes associated with principal radii a_i and b_i , significant spinal connections' lengths associated with x_i , significant twisting degrees associated with θ_i , and significant rotation of the material frame according to the tangent vectors associated with v_{1i} and v_{2i} , respectively.

global and partial hypothesis tests on ParkWest data comparing hippocampi of patients with Parkinson's disease (PD) versus a healthy control(CG), where in PD and CG we have 182 and 108 samples, respectively. As depicted in [Figure 11](#), there is a statistically significant difference between PD and CG based on the obtained p -value, which is 0.048, and the significant level of $\alpha = 0.05$. Further, [Figure 12](#) visualizes significant features that reflect the size, spinal elongation, degree of twist, and cross-sectional rotation with (bottom row) and without (top row) p -value adjustment.

6 Conclusion

In this work, we proposed a novel framework aimed at analyzing swept regions, particularly addressing the issue of self-intersection. We focused on a specific class of swept regions called elliptical slabular objects (E-SIOs). We introduced elliptical tube representation (ETRep) as a robust method for representing E-SIOs. The ETRep is invariant to rigid transformation and can be seen as a sequence of elliptical cross-sections along the object's center curve. To deal with the self-intersection problem in the ETRep analysis, we discussed the relative curvature condition (RCC). By considering the RCC, we defined ETRep space with an intrinsic skeletal coordinate system. We explained ETRep intrinsic distance and mean shape based on the introduced space. We introduced an intrinsic distance measure for the underlying shape space to avoid self-intersection and ensure valid statistics. We briefly outlined the issue of non-local intersections and proposed a solution for a specific class of ETReps that are simply straightenable. The advancement of the proposed solution, detailed in the Supplementary Materials, could serve as a focal point for future research. Finally, we demonstrated the application of ETRep analysis by comparing the hippocampi of patients with Parkinson's disease to those of a healthy control group.

Acknowledgments

This work is funded by the Department of Mathematics and Physics of the University of Stavanger (UiS). We thank Prof. James Damon (late of UNC) for the inspiration of this work. We also thank Prof. Guido Alves (UiS) for providing the ParkWest data.

SUPPLEMENTARY MATERIALS

Supplementary: Supplementary Materials referenced in this work are available as a pdf.

R-code: In Supplementary.zip, R codes and files are placed. (zip)

References

Abbena E, Salamon S, Gray A (2017) Modern differential geometry of curves and surfaces with Mathematica. CRC press

- Alves G, Müller B, Herlofson K, HogenEsch I, Telstad W, Aarsland D, Tysnes OB, Larsen JP (2009) Incidence of parkinson's disease in norway. the norwegian parkwest study. *Journal of Neurology, Neurosurgery & Psychiatry*
- Amaral GA, Dryden I, Wood ATA (2007) Pivotal bootstrap methods for k-sample problems in directional statistics and shape analysis. *Journal of the American Statistical Association* 102(478):695–707
- Apostolova L, Alves G, Hwang KS, Babakchianian S, Bronnick KS, Larsen JP, Thompson PM, Chou YY, Tysnes OB, Vefring HK, et al. (2012) Hippocampal and ventricular changes in parkinson's disease mild cognitive impairment. *Neurobiology of aging* 33(9):2113–2124
- Bærentzen A, Rotenberg E (2021) Skeletonization via local separators. *ACM Transactions on Graphics (TOG)* 40(5):1–18
- Ballard D, Brown C (1982) Representations of three-dimensional structures. *Computer Vision* pp 264–311
- Benjamini Y, Hochberg Y (1995) Controlling the false discovery rate: a practical and powerful approach to multiple testing. *Royal Statistical Society* 57:289–300
- Brady M, Asada H (1984) Smoothed local symmetries and their implementation. *The International Journal of Robotics Research* 3(3):36–61
- do Carmo M (2016) *Differential Geometry of Curves and Surfaces: Revised and Updated Second Edition*. Dover Books on Mathematics, Dover Publications
- Carroll D, Köse E, Sterling I (2013) Improving frenet's frame using bishop's frame. arXiv preprint arXiv:13115857
- Damon J (2003) Smoothness and geometry of boundaries associated to skeletal structures i: Sufficient conditions for smoothness. In: *Annales de l'institut Fourier*, vol 53, pp 1941–1985
- Damon J (2008) Swept regions and surfaces: Modeling and volumetric properties. *Theoretical Computer Science* 392(1-3):66–91

- Dryden I, Mardia K (2016) *Statistical Shape Analysis: With Applications in R*. Wiley Series in Probability and Statistics, Wiley
- Fletcher PT, Lu C, Pizer SM, Joshi S (2004) Principal geodesic analysis for the study of nonlinear statistics of shape. *IEEE transactions on medical imaging* 23(8):995–1005
- Gamble J, Heo G (2010) Exploring uses of persistent homology for statistical analysis of landmark-based shape data. *Journal of Multivariate Analysis* 101(9):2184–2199
- Gamelin T, Greene R (1999) *Introduction to Topology*. Dover books on mathematics, Dover Publications, URL <https://books.google.no/books?id=thAHAGyV2MQC>
- Georgiades P (1992) Plane-to-plane intersection. In: *Graphics Gems III (IBM Version)*, Elsevier, pp 233–235
- Giomi L, Mahadevan L (2010) Statistical mechanics of developable ribbons. *Physical review letters* 104(23):238104
- Guillemin V, Pollack A (2010) *Differential Topology*. AMS Chelsea Publishing, AMS Chelsea Pub., URL <https://books.google.no/books?id=FdRhAQAAQBAJ>
- Huynh DQ (2009) Metrics for 3d rotations: Comparison and analysis. *Journal of Mathematical Imaging and Vision* 35(2):155–164
- Jermyn I, Kurtek S, Laga H, Srivastava A, Medioni G, Dickinson S (2017) *Elastic Shape Analysis of Three-Dimensional Objects*. Synthesis Lectures on Computer Vision, Morgan & Claypool Publishers, URL <https://books.google.no/books?id=oq42DwAAQBAJ>
- Jung S, Dryden IL, Marron J (2012) Analysis of principal nested spheres. *Biometrika* 99(3):551–568
- Kendall DG (1984) Shape manifolds, procrustean metrics, and complex projective spaces. *Bulletin of the London Mathematical Society* 16(2):81–121
- Laga H, Guo Y, Tabia H, Fisher R, Bennamoun M (2019) *3D Shape Analysis: Fundamentals, Theory, and Applications*. Wiley

- Lee J (2013) Introduction to Smooth Manifolds. Graduate Texts in Mathematics, Springer
New York, URL <https://books.google.no/books?id=w4bhBwAAQBAJ>
- Lele SR, Richtsmeier JT (2001) An invariant approach to statistical analysis of shapes.
Chapman and Hall/CRC
- Lu Y (2013) Discrete frenet frame with application to structural biology and kinematics.
PhD thesis, The Florida State University
- Ma R, Zhao Q, Wang R, Damon J, Rosenman J, Pizer S (2018a) Deforming generalized
cylinders without self-intersection by means of a parametric center curve. Computational
Visual Media 4:305–321
- Ma R, Zhao Q, Wang R, Damon JN, Rosenman JG, Pizer SM (2018b) Skeleton-based
generalized cylinder deformation under the relative curvature condition. In: PG (Short
Papers and Posters), pp 37–40
- Mardia K, Bibby J, Kent J (1982) Multivariate analysis. Probability and mathematical
statistics, Acad. Press
- Moakher M (2002) Means and averaging in the group of rotations. SIAM journal on matrix
analysis and applications 24(1):1–16
- O’Searcoid M (2006) Metric Spaces. Springer Undergraduate Mathematics Series, Springer
London, URL <https://books.google.no/books?id=aP37I4QWFRcC>
- Pennec X, Sommer S, Fletcher T (2019) Riemannian Geometric Statistics in Medical Image
Analysis. Elsevier Science
- Pizer SM, Jung S, Goswami D, Vicory J, Zhao X, Chaudhuri R, Damon JN, Huckemann
S, Marron J (2013) Nested sphere statistics of skeletal models. In: Innovations for Shape
Analysis, Springer, pp 93–115
- Pizer SM, Marron J, Damon JN, Vicory J, Krishna A, Liu Z, Taheri M (2022) Skeletons,
object shape, statistics. Frontiers in Computer Science 4:842637
- Rizzo M (2007) Statistical Computing with R. Chapman & Hall/CRC The R Series, Taylor
& Francis, URL <https://books.google.no/books?id=BaHhdq0ugjsC>

- Rustamov RM, Lipman Y, Funkhouser T (2009) Interior distance using barycentric coordinates. In: Computer Graphics Forum, Wiley Online Library, vol 28, pp 1279–1288
- Schulz J, Pizer SM, Marron J, Godtlielsen F (2016) Non-linear hypothesis testing of geometric object properties of shapes applied to hippocampi. *Journal of Mathematical Imaging and Vision* 54(1):15–34
- Siddiqi K, Pizer S (2008) Medial Representations: Mathematics, Algorithms and Applications. *Computational Imaging and Vision*, Springer Netherlands
- Srivastava A, Klassen E (2016) Functional and Shape Data Analysis. Springer Series in Statistics, Springer New York
- Styner M, Oguz I, Xu S, Brechbühler C, Pantazis D, Levitt JJ, Shenton ME, Gerig G (2006) Framework for the statistical shape analysis of brain structures using spharm-pdm. *The insight journal* 1(1071):242
- Taheri M, Schulz J (2022) Statistical analysis of locally parameterized shapes. *Journal of Computational and Graphical Statistics* 0(ja):1–28
- Taheri M, Pizer SM, Schulz J (2023) Fitting the discrete swept skeletal representation to slabular objects, URL <https://doi.org/10.21203/rs.3.rs-2927062/v1>, submitted
- Van Kaick O, Zhang H, Hamarneh G, Cohen-Or D (2011) A survey on shape correspondence. In: Computer graphics forum, Wiley Online Library, vol 30, pp 1681–1707
- Vouga E (2014) Lectures in discrete differential geometry 1–plane curves
- Wei S, Lee C, Wichers L, Marron J (2016) Direction-projection-permutation for high-dimensional hypothesis tests. *Journal of Computational and Graphical Statistics* 25(2):549–569
- Yang K, Ke C, Tian J, Liu J, Guo Z, Liu D (2022) Three-dimensional curve reconstruction based on material frame and twisted multicore fiber. *IEEE Photonics Journal* 14(6):1–8